

Ice Particle Properties Inferred from Aggregation Modelling

Markus Konrad Karrer^{1,1}, Stefan Kneifel^{2,2}, Davide Ori^{3,3}, Christoph Siewert^{4,4}, Axel Seifert^{4,4}, and Annakaisa von Lerber^{5,5}

¹Institute of Geophysics and Meteorology

²University of Cologne

³Institute for Geophysics and Meteorology

⁴Deutscher Wetterdienst

⁵Finnish Meteorological Institute

November 30, 2022

Abstract

We generated a large number (105'000) of aggregates composed of various monomer types and sizes using an aggregation model. Combined with hydrodynamic theory, we derived ice particle properties such as mass, projected area, and terminal velocity as a function of monomer number and size. This particle ensemble allows us to study the relation of particle properties with a high level of detail which is often not provided by in-situ measurements. The ice particle properties change rather smoothly with monomer number. We find very little differences in all particle properties between monomers and aggregates at sizes below 1 mm which is in contrast to many microphysics schemes. The impact of the monomer type on the particle properties decreases with increasing monomer number. Whether e.g., the terminal velocity of an aggregate is larger or smaller than an equal-size monomer, depends mostly on the monomer type. We fitted commonly used power laws as well as Atlas-type relations, which represent the saturation of the terminal velocity at larger sizes, to the dataset and tested the impact of incorporating different levels of complexity with idealized simulations using a 1D Lagrangian super-particle model. These simulations indicate that it is sufficient to represent the monomer number dependency of ice particle properties with only two categories (monomers and aggregates). The incorporation of the saturation velocity at larger sizes is found to be important to avoid an overestimation of self-aggregation of larger snowflakes.

Ice Aggregate Properties Emergent from Aggregation Modelling

. n ¹ A e ² . e ² . i ¹ A b ^{1,3} . b ¹

¹ I f C h M C h C h C n
² I h M C n
³ F h M h H h F h

d

We simulated aggregates to study the impact of monomer number and type on ice particle properties

Ice particle properties show a smooth transition from monomers to aggregates

The saturation of terminal velocity needs to be taken into account when simulating snow aggregation

Abstract

We generated a large number 105,000 of aggregates composed of various monomer types and sizes using an aggregation model. Combined with hydrodynamic theory, we derived ice particle properties such as mass, projected area, and terminal velocity as a function of monomer number and size. This particle ensemble allows us to study the relation of particle properties with a high level of detail which is often not provided by in-situ measurements. The ice particle properties change rather smoothly with monomer number. We find very little differences in all particle properties between monomers and aggregates at sizes below 1 mm which is in contrast to many microphysics schemes. The impact of the monomer type on the particle properties decreases with increasing monomer number. Whether e.g., the terminal velocity of an aggregate is larger or smaller than an equal-size monomer, depends mostly on the monomer type. We tested commonly used power laws as well as Atlas-type relations, which represent the saturation of the terminal velocity at large sizes (terminal velocity asymptotically approaching a limiting value), to the dataset and tested the impact of incorporating different levels of complexity with idealized simulations using a 1D Lagrangian super-particle model. These simulations indicate that it is sufficient to represent the monomer number dependency of ice particle properties with only two categories (monomers and aggregates). The incorporation of the saturation velocity at larger sizes is found to be important to avoid an overestimation of self-aggregation of larger snow flakes.

Introduction

We have simulated and analyzed the properties, such as mass, area, and terminal fall velocity of snow flakes using a computer model. The snow flakes in the atmosphere form by collisions of ice crystals present in many different shapes. In the computer model, ice crystals shapes typically found in the atmosphere, are stuck together to create three-dimensional snow flakes. The properties of the snow flakes depend on the shape and the number of ice crystals that are stuck together. While in weather and climate models the properties of ice crystals and snow flakes are often assumed to be very different even if they are of the same size, we find very little differences in their properties. Many weather and climate models assume that snow flakes have a higher fall velocity the larger they are, although field observations have shown that particles larger than a few mm all fall with similar velocity. We tested new parameterizations of the particle velocities which

can remove this deficiency in the models. Finally, we used another model and showed that it might be sufficient to divide the properties of the ice particles in only two categories. However, it is important to consider the almost constant velocity of the large snow flakes.

1.1

The terminal velocity v_m of ice monomers and aggregated ice particles and its relation to size has manifold impacts on precipitation and radiative effects of ice-containing clouds. For example, Morales et al. (2019) show that parameters describing v_m of aggregates have the largest impact on the precipitation of simulated orographic clouds. Experiments with global climate simulations revealed that also radiative fluxes are very sensitive to changes in v_m (Jakob, 2002). Sanderson et al. (2008) found, that v_m of ice is the second most influential parameter for the climate sensitivity in their multi-member perturbed physics General Circulation Model ensemble. Constraining v_m of cloud ice and aggregated ice particles can reduce the degrees of freedom in model tuning (e.g., to improve top of atmosphere radiative fluxes; Schmidt et al., 2017) and improve the physical consistency in atmospheric models.

The importance of v_m of ice particle has been early recognized and has motivated first observational studies in the first third of the 20th century. Using initially manual observations and microphotography, pioneering studies such as Nakaya and Terada (1935); Langleben (1954); Brown (1970); Zikmunda and Vali (1972); Kajikawa (1972); Locatelli and Hobbs (1974) investigated the relation of v_m to the particle's size for various ice particle habits and aggregates. In addition to the direct measurements of velocity, several studies started to investigate the principle relation between particle properties such as mass, size, and projected area to v_m which allows deriving v_m from these quantities (Cornford, 1965; Heymsfeld, 1972). Due to the large efforts in performing these often manual measurements, the sample size of the derived relations is rather small. For example, some of the widely used relations by Locatelli and Hobbs (1974) are only based on 10 to 50 particles. One can assume that particles with ideal monomer types might have been subjectively chosen in order to easier associate the derived relationships to certain well defined shapes. Nevertheless, the relations of size, mass, area, and v_m derived in these early studies are still used in microphysics parameterizations (e.g. the v_m size relation of the snow category in Morrison and Milbrandt (2015) is

taken from Locatelli and Hobbs (1974) mixed aggregates; see Figure 1). In Figure 1a a selection of the aforementioned v_{tm} relations are shown for their defined size range. The spread of velocities for different ice particle monomers is relatively high (e.g. Kajikawa (1972) reported v_{tm} to be about 0.2 m s^{-1} for a dendrite but about 0.5 m s^{-1} for a plate monomer). In contrast v_{tm} of aggregates of different monomer types appear to be relatively similar and always close to 1 m s^{-1} in the reported size range.

Evolving computer technology allowed the realization of automated particle measurement systems such as the 2D Video Disdrometer (2DVD, Kruger and Krajewski (2002)), the Snow Video Imager (SVI; Newman et al., 2009), its successor the Particle Imaging Package (PIP Tiira et al., 2016), the Hydrometeor Velocity and Shape Detector (HVSD; Barthazy et al., 2004), or the Multi-Angle Snowflake Camera (MASC; Garrett et al., 2012). These systems are based on optical methods to capture particle size and terminal velocity. Unlike in the early studies, particle property relations (Barthazy & Schefold, 2006; Brandes et al., 2008; Zawadzki et al., 2010; Garrett & Yuter, 2014b) are now based on a very large number of particles which are classified by automated algorithms rather than visual selection (Bernauer et al., 2016; von Lerber et al., 2017). All optical disdrometers have a smallest detectable size limit (e.g., 0.1-0.2 mm for 2DVD), which implies that measurements close to this limit should be interpreted with care. A general behavior, which is revealed by all instruments, is a 'saturation' of aggregate terminal velocities (i.e., terminal velocities asymptotically approaching a limiting value) at approximately 1 m s^{-1} for unrimed particles and sizes larger than a few millimeters (Figure 1a).

Most ice microphysics schemes use two categories for unrimed ice particles, which are commonly denoted as cloud ice and snow/aggregates. Relations between particle properties, such as size (e.g. the maximum dimension $D_{m, \max}$), mass m , projected area A , or v_{tm} are defined for each category. Examples of the v_{tm} dependence on size which are implemented in widely used two-moment schemes are shown in Figure 1b. When comparing these relations with observations (Figure 1a), we miss the saturation behavior of v_{tm} for larger sizes in most relations. This discrepancy is expected as most schemes use power laws, which are unable to represent a saturation behavior. Alternative 'Atlas-type' three-parameter fits have been suggested (Seifert et al., 2014) but so far they have not been tested thoroughly. The recent Predicted Particle Properties (P3) scheme (Morrison & Milbrandt, 2015) uses only one ice category and a look-up table approach for v_{tm} which better matches the saturation at large sizes. At the smaller size range, the snow

category is found for all schemes to fall significantly faster than the ice category with the same size. Considering that v_m depends strongly on m and A of the particle, it might sound plausible, that for example, an aggregate of a few plates should fall faster than a single plate of the same size. Unfortunately, most observations do not provide sufficiently detailed information about monomer number and type which would be needed to answer the question of whether there exists a 'jump' in v_m for the number of monomers exceeding a certain threshold. Fairly direct observations of the particles and A are only available from manual, particle-based observations (e.g. Locatelli & Hobbs, 1974).

An interesting new tool to better understand the underlying principles of aggregation and its effects on particle properties are aggregation models (Westbrook et al., 2004a; Hashino & Tripoli, 2011; Leinonen & Moisseev, 2015; Ori et al., 2014; Prybylo et al., 2019). Those models use idealized monomer shapes (e.g., dendrites, needles, plates, columns) with particle properties matched to in-situ observations. Aggregates simulated with the model by Westbrook et al. (2004a) helped to better understand theoretical scaling relations associated to aggregation such as the increase of aggregate mass with size by a power of two (Westbrook et al., 2004b), which was known from several previous in-situ observations. This model has been extended by Leinonen and Moisseev (2015) providing a large number of monomer shapes and also provides an option to rime the aggregate (Leinonen & Syrmer, 2015). This allowed to better understand the evolution of size and mass of a large number of aggregates which were increasingly rimed (Seifert et al., 2019).

To infer v_m from modeled ice particles or aggregates, computational fluid dynamics is an accurate but also computational costly method. It has been recently applied to idealized ice particle shapes (Hashino et al., 2016; Nettlesheim & Wang, 2018; Burgesser et al., 2019) and more computations with more complex shapes can be expected shortly. Hydrodynamic theory is a computational cheaper alternative to calculate v_m based on a number of bulk particle characteristic, rather than the complex 3D-shape (e.g. Ohm, 1992; Khvorostyanov & Curry, 2005; Heymsfeld & Westbrook, 2010). The accuracy of hydrodynamic theories has recently been evaluated by ice particle analogs falling in an oil tank (Westbrook & Sephton, 2017). The experimental results show deviations smaller than 20% for the Heymsfeld and Westbrook (2010) theory. A problematic aspect of these theories is still the formulation of the scaling towards higher Reynolds num-

ber (i.e. large particles) and the simulation of more complex particle shapes (Westbrook & Sephton, 2017).

Aggregation models in combination with hydrodynamic theory have recently been used to study v_m of aggregates (Hashino & Tripoli, 2011; Schmitt et al., 2019). Hashino and Tripoli (2011) identified a dependency of the aggregation rate and aggregate mass on the mean size and type of the monomers. Schmitt et al. (2019) analyzed v_m and its variability of simulated aggregates composed of hexagonal prisms taken from a monodisperse monomer size distribution. They found that the variability of v_m is caused by the variability of the number of monomers N_m and the monomers' aspect ratio.

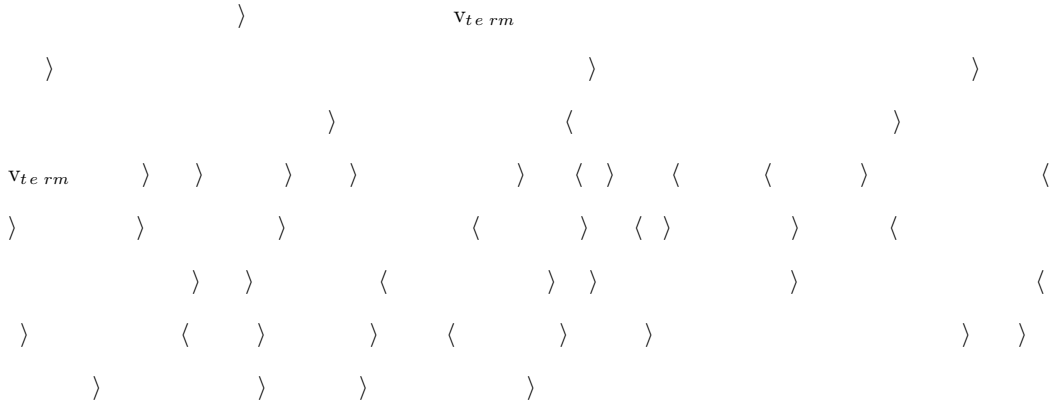
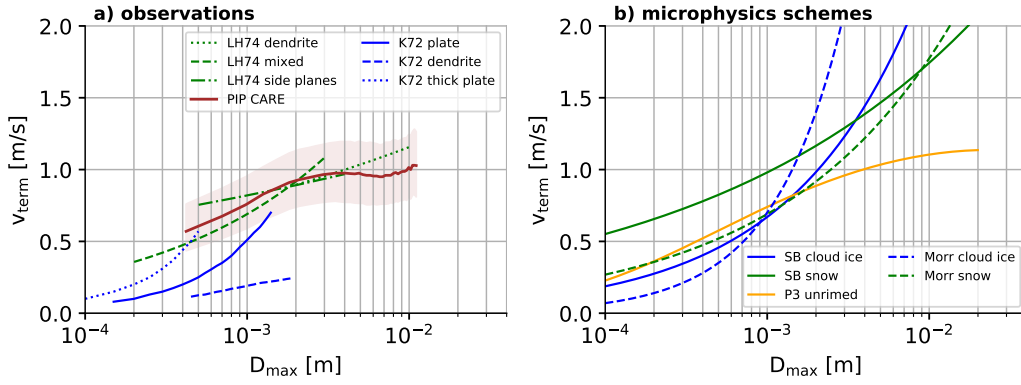
In this study, we aim to study the dependency of A and v_m on size, monomer number and type. For this, we create a large number of aggregates with various monomer types including also mixtures of different monomer types. The monomer size is sampled from a size distribution rather than a constant size to better represent real ensembles of aggregates. Central questions of this study are, how important is the monomer number and type information for parameterizing aggregate properties and how well can they be parameterized by different functional relations?

To answer these questions, we describe in Section 2 the aggregation model and the created dataset of unrimed aggregates as well as the hydrodynamic theory to calculate v_m based on m and A of these particles. The simulated particle properties are compared to in-situ observations in Section 3. Section 4 presents several parameterizations of the particle properties. Finally, in Section 5, we use a 1D Lagrangian particle model to test the impact of including different complexity of particle properties for aggregation

2 e

2.1

We use the aggregation model developed by Leinonen and Moisseev (2015) which includes a large number of realistic monomers (hexagonal plates, dendrites, columns, needle). Originally, the aggregation model was designed to produce realistic snow particle structures which can then be used to calculate their scattering properties (Leinonen & Moisseev, 2015; Leinonen et al., 2018). The model has also been used to systematically investigate microphysical processes, such as riming (Seifert et al., 2019).



The shape characteristics (length, thickness, etc.) of the monomers are prede ned by geometric relations based on in-situ observations (Leinonen & Moisseev, 2015). The aggregation process starts with generating N_m monomers with sizes following a prede ned inverse exponential probability density function $p(D_{mu})$

$$p(D_{mu}) = \exp(-D_{mu}) \quad (1)$$

where $^{-1}$ is the size parameter of the monomer distribution and D_{mu} is the maximum size of the monomer. The higher $^{-1}$ the larger are the sizes of the monomers.

The monomers sizes are sampled from the monomer distribution and assembled until an aggregate, consisting of N_m monomers is build up. In each aggregation step, pairs of particles are selected according to a simplified gravitational collection kernel. The probability distribution of collision among each possible particle pair is calculated as being proportional to the particle geometric cross sections and differential fall speed (Westbrook et al., 2004a). The two colliding particles form an aggregate which then becomes one of the candidates for the next aggregation step. This process includes the collision between

aggregates. The aggregation code is publicly available and more details on the implementation can be found in Leinonen and Moisseev (2015). During the aggregation process, the collecting particles are partially aligned with the principal axis in the x-y plane. Rotations around the principal axis are performed randomly with a standard deviation of 40° . The collected particles are randomly aligned, which mimics the complex flow in the vicinity of other particles (Leinonen & Moisseev, 2015).

The aggregation simulations performed in this study differ from previous studies in two main aspects. The first aspect is the resolution of the particle structure. The particle is internally represented by a three-dimensional lattice with a predefined distance of the volume elements of typically 40m. This distance was found to be sufficiently small for scattering computations, while being coarse enough in order to keep the numerical costs for the scattering computations in a reasonable range. However, we discovered that for small particle sizes, the theoretical relations for certain particle properties (see Figure 1 in Leinonen and Moisseev (2015)) are not exactly matched by the discretized particle. This discrepancy can be easily explained when considering for example that plate monomers with $D_m < 3.03$ mm consist of only one layer of volume elements if the default resolution of 40 m is used. This does not necessarily affect the aggregate properties of those monomers as shown in Leinonen and Moisseev (2015), however, in our study, the focus is to investigate the transition from small to larger size particles. Hence, we need to refine the resolution especially for small particles.

As a compromise between computational feasibility and having fine enough resolved particles, aggregates with $N_m < 100$ are simulated with a resolution of 5m, while aggregates with $N_m > 100$ are simulated with 10 m resolution. With a resolution of 5 m (10 m) a plate monomer with $D_m = 3$ mm has a thickness of 4 (8) volume element layers. It should be noted that the sensitivity to resolution is smaller for monomer types with less extreme aspect ratios (e.g. columns).

The second major difference to previous aggregation studies using the model by Leinonen and Moisseev (2015) is that we extended the code in a way that we can also generate aggregates composed of monomers with different habits. The motivation for this new feature was based on observations that larger snowflakes often consist of a mixture

¹ <https://github.com/jleina/aggregation>

$$A D_{m,x} ; N_{no} \quad a_{m,1} D_{m,x}^{b_{m,1}} \quad N_{mno} \quad a_{A,1} D_{m,x}^{b_{A,1}}$$

Monomer type	$a_{m,1}$ [kgm ^{-m}]	$b_{m,1}$	$a_{A,1}$ [m ² m ^{-A}]	$b_{A,1}$
Plate	0.788	2.48	0.631	1.99
Needle	0.005	1.89	0.002	1.42
Dendrite	0.074	2.33	0.142	1.94
Column	0.046	2.07	0.008	1.54

of dendrites and needles (Lawson et al., 1998). The modified code extends Equation 1 to be the joint distribution of multiple mono-dispersed distributions. Each monomer distribution is defined by its own settings (e.g., monomer type, mean size and truncation). The joint distribution is defined by the relative weights of each mono-dispersed distribution. These modifications have been merged to the main aggregation code and are also publicly available.

In order to account for a large variability of naturally observed particle shapes (Bailey & Hallett, 2009), we simulated a large suite of aggregates consisting of plates, columns, dendrites, needles and mixtures of dendrites and columns. The $D_{m,x}$ and $A D_{m,x}$ relations for the monomers are given in Table 1. Two sets of aggregates with mixed monomer types were created. For the first mixture, the selection of the monomer type is random with the same probability density function for both monomer types ("Mix1"). This would represent a scenario, where dendrites and needles coexist with similar PSD and likelihood of aggregation. For the second mixture, the monomers with $D_{m,x} < 1$ mm are columns, while dendrites are taken for larger monomers ("Mix2"). This choice is motivated by the fact that at temperatures below -20°C, the particle shape is less distinct but mostly described by polycrystals while at temperatures between -20 and -10°C one finds more planar and dendritic crystals (Bailey & Hallett, 2009). Considering a thick cloud, we could assume that the small polycrystal or columnar crystals forming in the

Resolution	τ^{-1}	N_m	D_m of the aggregate
5 m	50 m - 10 mm	1,2,3,...,10,20,30,...,100	1-2 cm
10 m	50 m - 10 mm	200,300,...,1000	3-5 cm

upper part of the cloud begin to form the first aggregate and then further grow by collection of larger dendrites at lower layers. Of course, both scenarios are quite ad-hoc and more detailed studies are needed to better understand the real properties of mixed-monomer aggregates. Our mixtures are thus rather intended to qualitatively analyze the differences of mixed monomer aggregates compared to single-monomer type aggregates (as done in another recent study by Dunnavan et al. (2019)).

The aggregation process strongly depends on the number concentration of particles and their relative terminal velocity differences. In conditions, which are less favorable for aggregation (e.g., low number concentration) the particles can grow by depositional growth to relatively large sizes before aggregation becomes the dominant process. It is therefore possible that aggregation involves very different monomer sizes. In order to account for this variability, we vary τ^{-1} in a large range from 50 m to 10 mm with 500 different values of τ^{-1} , spaced evenly in the logarithmic space. The monomer distribution is limited to sizes of 100 μ m up to 3 mm following Leinonen and Moisseev (2015) in order to be consistent with the typical size range of observed ice particles. Due to this truncation of the inverse exponential distribution, the mean monomer size differs from τ^{-1} and ranges from 150 μ m to 1.48 mm.

The spacing of the monomer number (Table 2) is finer at low N_m and becomes more coarse at larger numbers. In this way, we can investigate the changes at small monomer numbers with greater detail. In fact, we expect the largest changes in snow properties at the transition from single monomers to aggregates composed of few pristine crystals as shown in earlier studies (Schmitt & Heymsfield, 2010; Dunnavan et al., 2019). The coarser spacing of N_m also limits computational costs. With our settings we obtain maximum aggregates sizes ranging from 3 cm to 5 cm which means that we include also



the typically observed large snow flakes during intense snowfall on the ground (Lawson et al., 1998).

In Figure 2 several examples of similar sized aggregates simulated with different combinations of r^{-1} , N_m , and monomer types are shown. In total, 105,000 particles were simulated. Apart from the visual differences of shapes and structure, also the particle properties such as mass, area, or terminal velocity show a wide range of values although all aggregates have maximum sizes ranging between 3 and 5 mm.

2.2 ~~is~~

Hydrodynamic models are needed in order to derive the terminal velocity v_m from the particle's mass m , projected area A and maximum size D_m . The most commonly used hydrodynamic models are Bhm (1992, hereafter B92), Khvorostyanov and Curry (2005, hereafter KC05) and Heymseld and Westbrook (2010, hereafter HW10). All models are based on particle boundary layer theory and rely on the Best number X (approach (Abraham, 1970)). v_m is calculated via

$$v_m = \sqrt{\frac{X}{\rho_a D_m}} \quad (2)$$

where μ is the dynamic viscosity, Re the Reynolds number (parameterized as a function of X) and ρ_a is the air density. X is defined as

$$X = C Re^2 \quad (3)$$

where C is the drag coefficient. The proportionality of X to the particle properties is given by

$$X = m D_m^{0.5} A^{-0.5} \quad (4)$$

for B92.

For this study, we decided to use B92 because it best represents the saturation of v_m for our simulated particles at larger aggregate sizes (Figure A2) in accordance with observations (Figure 1). B92 includes an empirical correction X due to wake turbulence which increases the drag of large particles. X depends on the aspect ratio α , which is larger than one for prolate and smaller than one for oblate particles. For this study, we set α to 1:0, because aggregates with small values of α are not easily classifiable as either prolate or oblate and show in general a large variability of α (Jiang et al., 2019).

To be able to interpret the dependency of v_m on N_m in Section 4.3, we sketch here how v_m scales with D_m in the simplified case of $Re \ll 1$ (Stokes drag) and $Re \gg 1$ (Newtonian drag). For $Re \gg 1$, C_D is approximately proportional to $1/Re$. Inserting this approximation and Equations 3 and 4 into Equation 2 yields:

$$v_m = \sqrt{\frac{X}{\rho_a D_m}} = \sqrt{\frac{m D_m^{0.5} A^{-0.5}}{\rho_a D_m}} \quad (5)$$

If we approximate m and A by the power laws $m = a_m D_m^m$ and $A = a_A D_m^A$, we can express v_m solely as a function of D_m :

$$v_m = C_D^{-1} D_{nw}^{m-0.5} A^{0.5} \quad (6)$$

For $Re \ll 1$, C_D is approximately constant. In this case Equation 3 gives $v_m \propto X^{0.5}$ and by using again the Equations (2 and 4) we get:

$$v_m = m D_{nw}^{-1.5} A^{-0.5} X^{0.5} = D_{nw}^{m-1.5} A^{0.5} X^{0.5} \quad (7)$$

In both extreme cases of $Re \ll 1$, v_m increases the faster with size the higher Re is and we expect this also to be in between these cases where Re transitions from $Re \ll 1$ to $Re \gg 1$. This has certain implications for the dependency of v_m on N_m (Section 4.3).

The differences between the three hydrodynamic models as well as an analysis of the potential impact of changing to different hydrodynamic models is discussed in the Appendix A2.

3.1.1. Particle size

3.1.1. Particle size

Particle properties, such as m , A and D_{nw} , are used in hydrodynamic models to calculate v_m (Section 2.2). We compare our relations of these particle properties and v_m with frequently used relations that are based on in-situ measurements from Locatelli and Hobbs (1974, LH74) and Mitchell (1996, M96). LH74 defined an equivalent diameter, that is equal to "the diameter of the smallest circle into which the aggregate as photographed will fit without changing its density". M96 collected observations as a function of D_{nw} without specifying the exact definition. The definitions of particle size used in these studies are limited by the observation equipment used and the conversion from one to the other is not trivial. In our simulation study we can access the full 3D structure of the particles and use the true maximum size (i.e. the maximum distance between any two points of the particle) as size definition.

Except for the aggregates of dendrites, which have a considerably lower density than LH74 aggregates of dendrites, the absolute value of the simulated aggregates is similar to the observations, where the same monomer type is available (Figure 3). The slope of the $m \propto D_{nw}$ relation from this study is comparable to the slope from M96, while

LH74 report lower slopes for the aggregates of dendrites. The D_{nu} relation of the mixed aggregates ("Aggregates of unrimed radiating assemblages of plates, side planes, bullets, and columns", LH74 mix), however, has a similar slope to the simulated Mix2 aggregates. The mixS3 and sideplane aggregates from M96 are similar to many simulated aggregates (composed of different monomers).

M96 derived A D_{nu} relations for "assemblages of planar polycrystals in cirrus clouds" (M96 polycrystal in Figure 3) based on observations in a relatively small size range and applied them to other aggregate types. This D_{nu} relation is also used in several microphysics schemes (Morrison & Milbrandt, 2015; Brdar & Seifert, 2018). The absolute value of A given in M96 is slightly higher than A of the simulated particles from this study (except for the aggregates of plates). The slope of the D_{nu} relations is slightly higher ($b_A = 1.88$) in M96 observations compared to the relations from this study ($1.79 < b_A < 1.88$). Observations of aggregates composed of the same monomer types than the one used in these studies are not available.

3.2. ~~Eff~~

Observations of v_m vs. size have been reported using several different definitions of the diameter (Syrrmer & Zawadzki, 2010). To facilitate a consistent comparison between the observations from the PIP instrument (which are described in Section A1) and v_m of the simulated aggregates, we use the same bin sizes as the PIP instrument to derive the median v_m . Moreover we derive the maximum dimension from a side projection of the modeled particle in the same way as in the observations from the PIP instrument (described by von Lerber et al., 2017) ($D_{max,s}$; Figure 3c,d). Displayed are the median and the 25 and 75 percentiles of v_m of the detected particles. Bins with fewer than 1000 particles are excluded from the statistics. Although LH74, M96 and Kajikawa (1972, K72) did not use the same definition as the PIP-CARE dataset, v_m from this study are also shown in Figure 3c and d because they can ease the comparison with other studies.

At small sizes ($D_{nu} < 1$ mm), v_m of the simulated aggregates of dendrites is close to v_m of the monomers from Kajikawa (1972, K72, Figure 3c). The plate monomers in K72 are reported with a similar v_m as the aggregates of plates, needles and Mix1 (which all have similar values). Note that v_m of plates and dendrites from K72 and

v_m of all aggregates simulated in this study (except for the aggregates of columns and "Mix2") are considerably smaller than v_m of the aggregates from the PIP-CARE dataset and LH74. The observations from LH74 are within the 25th and 75th percentile of the PIP-CARE dataset. The median of v_m of the simulated aggregates of this study increases faster with size compared to the in-situ observations at sizes of several mm (Figure 3d). Only v_m of the mixture of small columns and large dendrites ("Mix2") have a comparably low slope. Potential reasons for this mismatch are limitations of the observations at these sizes (Brandes et al., 2008), turbulence affecting the observations (Garrett & Yuter, 2014b), missing processes in the aggregation model (e.g. depositional growth on aggregates), imperfect parameterizations in the hydrodynamic model, or the dominance of monomer type mixtures in the aggregates.

Figures 3c and d also show v_m calculated with B92 and then D_{nu} and A_{nu} relations from M96 (which did not measure v_m directly). The simulated slope of v_m from M96 observed aggregates is similar to the one simulated in this study while the absolute value is slightly higher.

At sizes larger than about 5 mm, the simulated and the observed v_m reach a saturation value close to 1 m s^{-1} . The median of v_m of most simulated aggregates lies within the 25th and 75th percentile in the sub-cm range, except the aggregates with the most extreme density (aggregate of dendrites and aggregates of columns). Thus, based on this comparison, these aggregates can be considered most representative for many aggregates found in the atmosphere.

4.1.1

The relationships between hydrometeor properties such as mass, size, projected area, and velocity are key components in any ice microphysics scheme and they strongly influence various microphysical processes (e.g., sedimentation, depositional growth, aggregation, or riming). Different microphysics schemes require a more or less simplified parameterization of particle properties. To address these different needs, we derive in this section v_m and A as a function of D_{nu} and N_m that can be used in microphysics schemes, which can predict v_m and N_m given a certain D_{nu} (Section 4.2). Of course, most bulk schemes require less detailed v_m and hence we also derive v_m of m , A , and v_m as a function of D_{nu} or the mass-equivalent diameter D_e . This also

allows us to assess the potential error of the less detailed models (Section 4.5) while their impact on modeled processes is studied later in Section 5.

4.1. Particle Properties

The particle properties of the monomers are defined a priori in the aggregation model and based on well-established observations. In contrast, the aggregate properties are determined by the aggregation process and change with increasing size. As we are particularly interested in quantifying how key particle properties of aggregates differ from the properties of the same-sized monomers, we normalize the aggregate properties by the property of a monomer with the same size.

$$f(D_{nu}; N_m) = \frac{p(D_{nu}; N_m)}{p(D_{nu}; N_m = 1)} \quad (8)$$

p represents the particle properties (mass or area) and $p(D_{nu}; N_m = 1)$ is the property of single monomers (given in Table 1), and f is the normalizing function. A normalizing function which is larger (smaller) than 1 indicates that the aggregate properties are larger (smaller) than its composing monomer with the same size (Figure 4).

To fit to various monomer types, we parameterize f by a power law and express the coefficients by rational functions to fit the dependency on N_m similar to the approach presented in Frick et al. (2013).

$$f(D_{nu}; N_m) = a(N_m) D_{nu}^{(N_m)} \\ = 10^{1 - \frac{a, p \log_1 N_m}{a, p \log_1 N_m}} D_{nu}^{\frac{b, p \log_1 N_m}{1 - b, p \log_1 N_m}} \quad (9)$$

The coefficients a and b for all monomer types can be found in Table 3. Note, that we excluded the mixture of monomer types from the monomer dependent analysis because our normalization approach cannot be applied to monomer mixtures.

4.2. Aggregate Properties

Motivated by the common classification of unrimed ice hydrometeors in cloud ice and snow in many bulk schemes, we will investigate in this section how mass and area change when building up an aggregate with an increasing number of monomers. In par-

ticular, we want to explore whether the properties change smoothly with monomer number or whether they show any sharp transition at certain monomer numbers.

When we compare the mass of an aggregate with the mass of its monomer of the same size, we find in some conditions the aggregate to be heavier or lighter than the monomer. The relevant mechanisms which explain this behavior are illustrated in Figure 4 for aggregates of plates. Note that we assume for simplicity a monodisperse monomer distribution in Figure 4. When we consider pure depositional growth, we obtain a specific D_m relation for each monomer type (Table 1; black line in Figure 4). One extreme aggregation scenario, which leads to the maximal size of an aggregate with a given number of monomers (which in this simplified case of a monodisperse distribution also determines its mass) would be if we assume that all monomers align along their maximum dimension. Clearly, the resulting aggregate would have a smaller size than a monomer of the same size. Of course, this maximal elongated assemblage of monomers is rather unlikely and thus the aggregate will have a more compact structure. If we imagine rearranging the monomers inside the aggregate in a progressively more packed configuration (indicated by the horizontal arrow in Figure 4), we might be able to reach the point where the size of the aggregate equals the one of the equal-mass monomer. At this point, it might be even possible to pack the monomers in a way that their size is smaller than an equal-mass monomer. A simple example of such an extreme packing would be to stack a number of plates on top of each other, i.e. along their smallest axis. Whether an aggregate can be smaller than an equal-mass monomer is of course also dependent on how close the monomer D_m relation is to the theoretical maximum packing of an equal-mass sphere.

The dependency of A on N_m can be understood analogously. Also for A , the maximal elongated assemblage of the monomers leads to a lower A of the aggregate compared to the monomer of the same size, but in reality, the monomers will assemble in a more compact way. In addition, we have to consider that A is not simply additive as it is the case for m . Overlap (in the horizontally projected plane) and non-horizontal alignment of the constituting monomers lead to a smaller A than the sum of A of the constituting monomers. Based on these simplified considerations it becomes clear that the dependency of m and A on N_m is determined by the exponent of the monomer power laws and the overall "compactness" of the aggregates.

When considering the monomer dependence of all simulated aggregates, we find the most different behavior for plate and needle aggregates. For plate aggregates, m and A steadily decrease for a given N_m with an increasing number of monomers (Figure 5b,d). From the principal considerations discussed in Figure 4, this behavior can be well understood. The plate monomers have the largest exponent ($\alpha_1 = 2.48$) of all monomers (Table 1) while the monomers itself show relatively loose connections within the aggregate (Figure 2a-c). Interestingly, the aggregate mass for very small N_m can be slightly larger than the equal-size monomer while A is immediately decreasing for $N_m > 1$. This effect can be easily understood when considering, for example, two plates that connect in a 90° angle of their major axes.

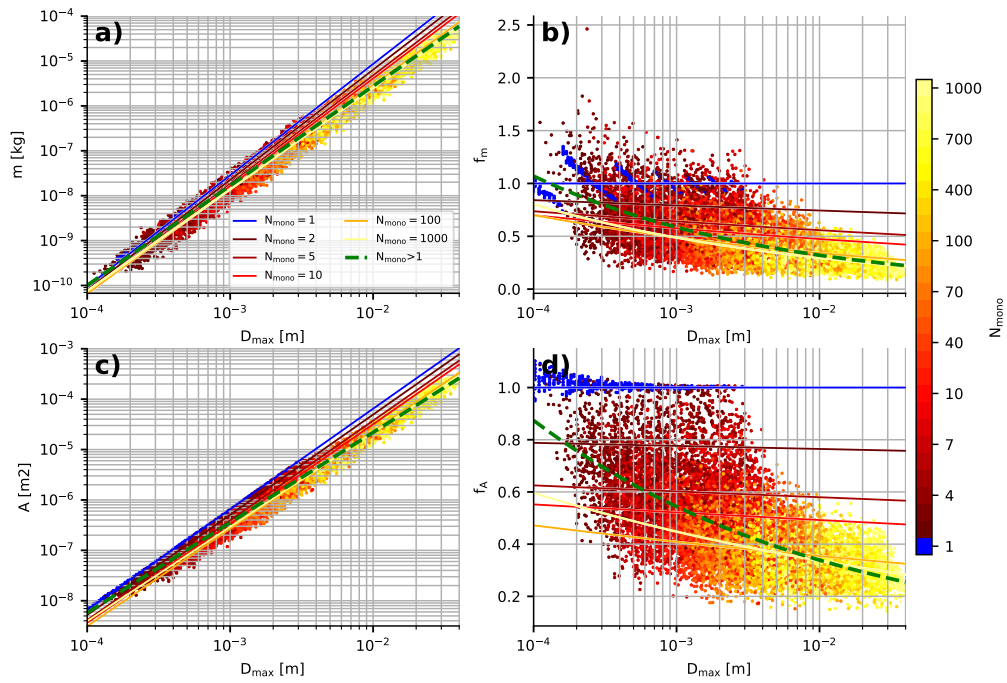
An opposite behavior is found for needle aggregates (Figure 6b,d). With increasing N_m , both m and A of the aggregates become larger than the equal-size monomers. In contrast to plates, the needle monomers have the lowest exponents for m and A power laws (Table 1). The aggregates of the more one-dimensional needles also show a more compact packing.

The deviation of the particle properties of the individual simulated particles from the fit is characterized by the mean absolute error (Table A2), which is smallest for plates (0.1190 for f_m and 0.0816 for f_A) and largest for needles (0.3737 for f_m and 0.3926 for f_A). The mean absolute error also shows that the monomer number dependent fit is superior to the more simple power law fit (Section 4.4) when there is a substantial dependence of the particle property on N_m .

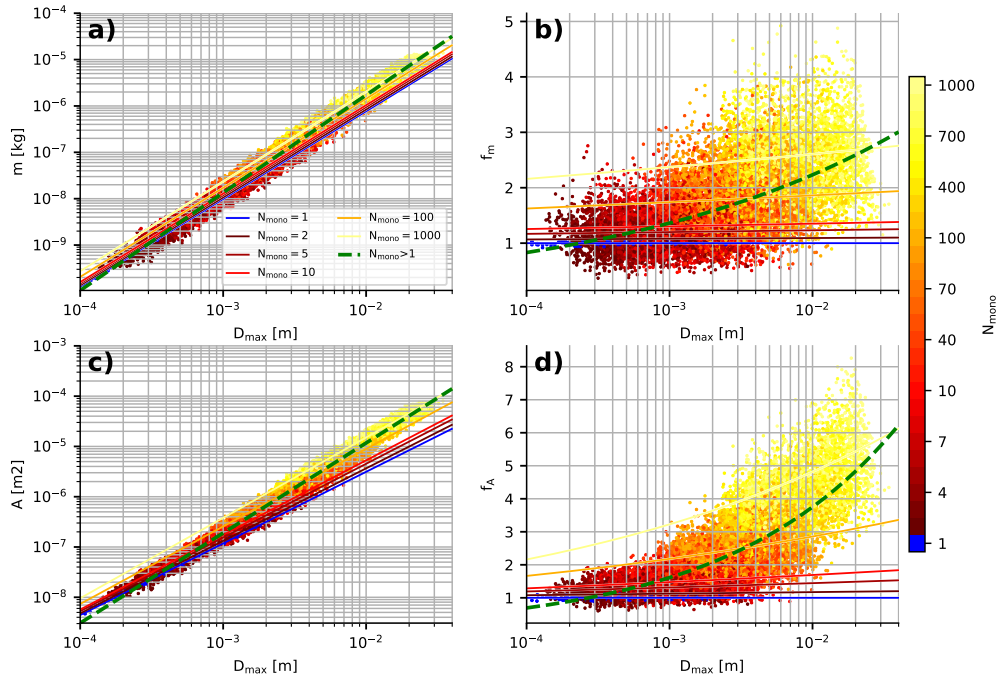
Dendrite and column aggregates have been analyzed similarly (according figures can be found in Supplement). The dendrites are similar to plates, while the columns are similar to needles. However, for all aggregate types, we find on average a relatively smooth transition of m and A when changing from single monomers to aggregates. For these two particle properties, we are unable to identify a "jump" due to the onset of aggregation. The next sections will show whether this behavior will change when deriving terminal velocity from m and A .

4.3. Terminal Velocity

The terminal velocity for all aggregates was calculated with the hydrodynamic model of B92 (Section 2.2). In Figure 7a, v_{∞} is shown as a function of N_m for plate ag-



m A $\langle \rangle$ D_{max} \langle
 $\rangle \rangle$ \rangle f_m f_A \rangle \rangle $\langle \rangle \rangle$ \langle
 m A $\rangle \langle$ D_{max} $\langle \rangle \rangle$ $\langle \rangle \rangle \rangle$
 \rangle $\rangle \langle \langle$ $\langle \rangle$ N_{mono} $\rangle \rangle$ m A N_{mono}
 \langle N_{mono}



gregates. Note, that the fits have been derived by applying B92 to the D_{max} and A D_{max} fits (Table 3) rather than fitting them directly to the cloud of individual m . In this way, we are consistent with the way how m – D_{max} relations are usually connected to m – D_{max} in bulk schemes. The terminal velocity of plate aggregates steadily decreases with increasing N_m . This dependency is much less pronounced at small D_{max} as compared to the largest sizes. However, it should be noted that the fits for very small monomer numbers are probably unrealistic for large D_{max} as we do not expect aggregates of cm sizes to be composed of only a few large plates. In fact, the here used geometrical relations for the plate monomers are only valid for a maximum size of 3 mm (Pruppacher & Klett, 1998).

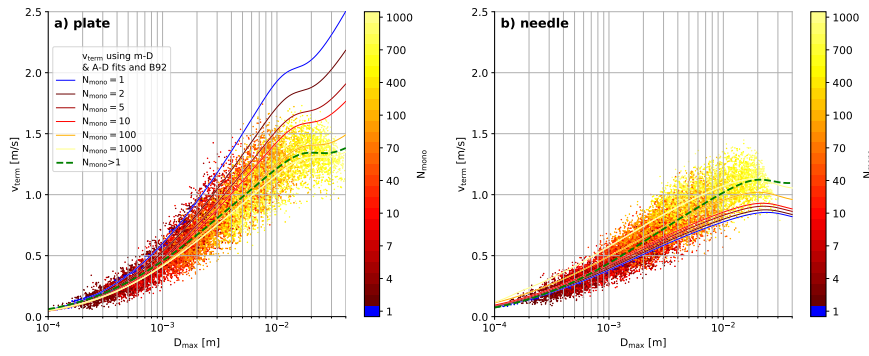
We find a similar decreasing f_m with increasing N_m for dendrites (see Supplement). As we might expect from the different change of m and A with N_m seen in Figure 7a, also the behavior of f_m with increasing N_m is different for needles (Figure 7). Needles aggregates seem to fall slightly faster when their monomer number increases. Interestingly, all aggregates reveal a very low dependence of f_m on monomer

number at small sizes which is in contrast to assumptions in some microphysics schemes, that distinguish between monomers and aggregates (e.g. Seifert & Beheng, 2006; Tsai & Chen, 2020). Besides, all aggregates reveal a saturation of v_m at large (centimeter) sizes which is in good agreement with observations (Figure 1). However, the absolute value of the saturation v_m ranges from 0.8 to 1.6 m s⁻¹ depending on the monomer type.

Because v_m of monomers and aggregates is converging towards the same value at small sizes (Figure 7), we can use the previously derived scaling relation (Equations 6 and 7) to relate the dependency of v_m on N_m to the exponents b_m and b_A of the monomers (b_{m-1} and b_{A-1}) and aggregates ($b_{m,agg}$ and $b_{A,agg}$) in the $m \propto D_m$ relation. Starting from a similar value of v_m at small sizes, v_m of an average aggregate increases slower than v_m of a monomer if $s_m = b_{m,agg} - b_{m-1} - 0.25(b_{A,agg} - b_{A-1}) < 0$ (cf. 6 and 7). As a result, at larger sizes, v_m of the aggregate is lower than v_m of the monomer. In an analog way v_m of an aggregate is larger than v_m of the monomer if $s_m > 0$. As $b_{m,agg}$ and $b_{A,agg}$ is similar for all aggregates (Table 4), the sign of v_m with increasing N_m depends mainly on b_{m-1} and b_{A-1} . For plates and needles, s_m equals 0.21 and 0.12, respectively.

How the particle properties change with increasing N_m as well as the absolute values of calculated v_m depends on the choice of the hydrodynamic model. Finding the optimal formulation of hydrodynamic models for ice and snow particles is still an active field of research (Westbrook & Sephton, 2017; Nettesheim & Wang, 2018) and outside the scope of this study. In Appendix A2, we tested the sensitivity of the results to the choice of the hydrodynamic model for plate aggregates. HW10 seems to yield overall similar results to B92 except for the saturation at large diameters. Due to the absence of the turbulence correction in HW10, v_m increases also at large diameters. For KC05, the monomer dependence is much weaker. However, all hydrodynamic models show an overall small monomer dependence at small particle sizes.

It has also been observed (e.g. Garrett & Yuter, 2014a) that tumbling of particles caused for example by turbulence might decrease the effective projected area and therefore increase v_m . We also tested the sensitivity of our results to different degrees of tumbling (Section A22). As expected, the effect of tumbling is largest for single crystals (due to their more extreme aspect ratio) but strongly decreases for aggregates. Certainly,



$$v_{term} \propto D_{max}^m \quad (1)$$

$$v_{term} \propto N_{mono}^n \quad (2)$$

$$N_{mono} \propto D_{max}^m \quad (3)$$

$$A \propto D_{max}^m \quad (4)$$

for aggregates, the choice of the hydrodynamic model has a larger effect of m than different assumptions on particle tumbling.

4.4. Aggregate

The relatively continuous change of particle properties with n found in the last section justifies a simplified fit, which is also necessary for implementing the results into common bulk microphysics schemes. These schemes often only contain two classes for unrimed ice particles, usually denoted as cloud ice (monomers) and snow (aggregates).

Figure 8a, b shows the derived D_{ma} relations for single monomers ($N_m = 1$) and the derived v_{m} based on them. D_{ma} and $A \propto D_{ma}$ relations summarized in Table 1. Similar fits of m and v_{m} to aggregates of any monomer number larger than 1 are shown in Figure 8c, d; the fit coefficients can be found in Table 4.

The $m \propto D_{ma}$ relations for monomers show a larger spread especially for larger sizes as compared to the aggregates. This is expected considering that the exponents for monomers range between 1.89 to 2.48 (Table 1) while the exponents for aggregates are between 1.95 and 2.22 (Table 4). The values for aggregates agree well with theoretical

$$a_{A,agg} D_{m,x}^{b_{A,agg}} \quad \langle \quad \rangle \quad a_{m,agg} D_{m,x}^{b_{m,agg}} \quad \langle \quad \rangle \quad A D_{m,x}$$

monomer type	$a_{m,agg}$ [kgm ^{-m}]	$b_{m,agg}$	$a_{A,agg}$ [m ² m ^{-A}]	$b_{A,agg}$
Plate	0.076	2.22	0.083	1.79
Needle	0.028	2.11	0.045	1.79
Dendrite	0.027	2.22	0.090	1.88
Column	0.074	2.15	0.060	1.79
Mix1	0.045	2.16	0.070	1.83
Mix2	0.017	1.94	0.066	1.79

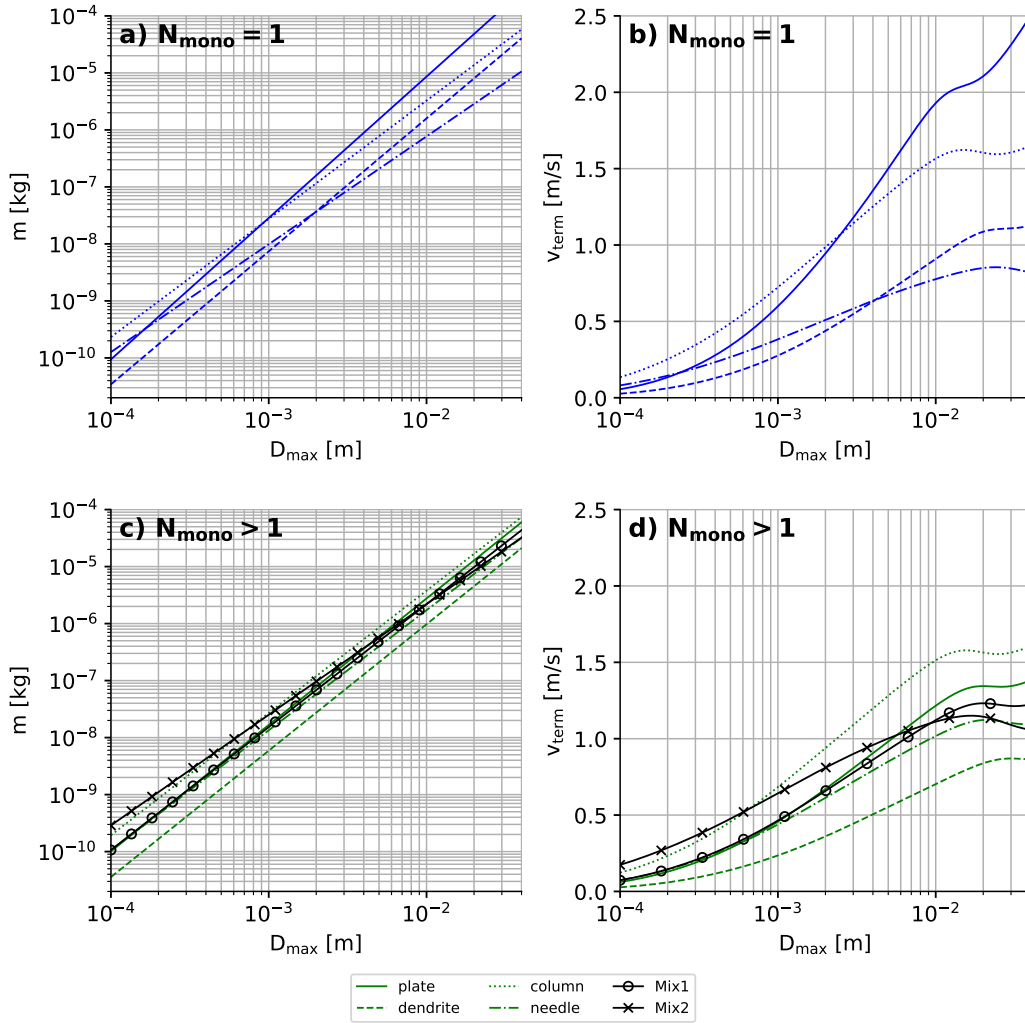
aggregation studies (Westbrook et al., 2004b) as well as in-situ observations (Section 3.1). Despite the similar exponent, the effective density of the aggregates varies considerably (compare at a given size in Figure 8c), which is in agreement with previous studies (Hashino & Tripoli, 2011; Dunnavan et al., 2019), even though their approaches to simulate aggregates is very different from the approach used in this study. Aggregates of columns exhibit the highest density, while aggregates of dendrites show the lowest density.

The differences in the D_{nu} relation are linked to the resulting v_m D_{nu} relation (Figure 8c, d). At $D_{nu} = 5$ mm, the v_m of different monomers spread nearly 1 m s^{-1} . The differences are in general smaller for aggregates. Interestingly, most aggregate types reveal very similar v_m . The main exceptions are dendrite aggregates with the slowest, and column aggregates with the fastest v_m . Of the Mix2 aggregates increases slower with increasing D_{nu} compared to the other aggregates.

Similar to the previous monomer number dependent fits, also the "two-category" fits show similar v_m at small sizes. The monomer type appears to have in general a much larger impact on v_m than the classification into certain N_m regimes.

4.5. Power-law fits

Power-law fits form, A , and v_m are commonly used in bulk schemes. Especially for v_m the power law introduces inconsistencies with observations because a satura-



$\langle \rangle$ m v_{term} $\langle \rangle$ D_{max} $\langle \rangle$ $\langle \rangle$
 $\langle \rangle$ m A D_{max} $\langle \rangle$ $\langle \rangle$ $\langle \rangle$
 $\langle \rangle$

tion value for v_m as observed for raindrops or snow flakes cannot be represented. Instead of using standard power laws in the form

$$v(D_{nu}) = a_v D_{nu}^x \quad (10)$$

and the two fit parameters a_v and b_v , Atlas et al. (1973) proposed a three-parameter (D_e , D_e , D_e) formulation

$$v_m(D) = D_e \exp(-D_e D) \quad (11)$$

Formulating this "Atlas-type" fit with the mass equivalent diameter D_m instead of D_{nu} has been found to provide optimal fit quality for snow aggregates (Seifert et al., 2014). For small (large) values of D , v_m approaches D_e (D_e). With increasing values of D , the transition from small to larger values of v_m is shifted towards larger values of D . Approximations for bulk collision rates based on Atlas-type fits can be found in Seifert et al. (2014) which makes them usable in bulk microphysics schemes without the necessity of look-up tables.

Power-law and Atlas-type relations have been applied to the various aggregates and the fit coefficients are summarized in Table 5. For the fitting, we did not use v_m of the individual particles but directly applied to v_m derived with B92 and the existing m_{nu} and A_{nu} relations.

In Figure 9 the different fits are compared for plate monomers and their aggregates. Note that the saturation region ($D_{nu} > 1$ cm) has been excluded for the power-law fits. It can be seen in Figure 9b that the Atlas-type fit is very close to the theoretical line calculated with B92 and the m_{nu} and A_{nu} relations. The power-law fits (Figure 9a) provide only a close fit to the theoretical values at the smaller size range. Between 300 μ m and 4 mm they cause a slight underestimation while at larger sizes they increasingly overestimate v_m . Similar fits have been derived for all aggregate types (Table 5, figures for other monomer types similar to Figure 9 can be found in the supplemental material).

When we compare the calculated v_m with some widely used microphysics schemes (Figure 9c) we find most schemes to overestimate v_m at small sizes (except of the cloud ice category in Morrison et al. (2005)). The absolute values for v_m at small sizes are strongly dependent on monomer type and hence, additional constraints should be pro-

Monomer type	D_e [m/s]	D_e [m/s]	D_e [1/m]	$a_{v, D_{ax}}$ [$m^{1-n_{ax}}$ /s]	$b_{v, D_{ax}}$
$N_m = 1$					
Plate	2.265	2.275	771.138	90.386	0.755
Needle	0.848	0.871	2276.977	9.229	0.481
Dendrite	1.133	1.153	1177.000	41.870	0.755
Column	1.629	1.667	1585.956	22.800	0.521
$N_m > 1$					
Plate	1.366	1.391	1285.591	30.966	0.635
Needle	1.118	1.133	1659.461	17.583	0.557
Dendrite	0.880	0.895	1392.959	24.348	0.698
Column	1.583	1.600	1491.168	23.416	0.534
Mix1	1.233	1.250	1509.549	21.739	0.580
Mix2	1.121	1.119	2292.233	8.567	0.393

vided by additional observations. However, the aggregation model shows independent on the monomer type that at sub-mm sizes there should be no strong "jump" in τ_m between ice particles and small aggregates. Also in the cm-size range, models using a power-law formulation are strongly overestimating τ_m for all aggregate types.

5 Model

In this section, we will test the possible impact of implementing particle properties with different amount of complexity (monomer number dependence) or different settling functions (power law vs Atlas type) on the simulation of sedimentation, aggregation and depositional growth. For this, we use a one-dimensional setup of the Lagrangian particle model McSnow (Brdar & Seifert, 2018), which provides the flexibility to implement the different particle property formulations.

For simplicity, only sedimentation, depositional growth and aggregation are considered in our simulations. Aggregation is calculated with a Monte-Carlo algorithm fol-

lowing Shima et al. (2009) and the sticking efficiency of Connolly et al. (2012) is used. McSnow is based on the Lagrangian super-particle approach (Shima et al., 2009), which allows deriving not only the particle mass and its multiplicity N_m , but it also predicts the number of monomers the particle is composed of. This information is key to test the N_m dependent particle relations. The thermodynamic profiles and the overall setup is similar to previous simulation studies with McSnow in Brdar and Seifert (2018) and Seifert et al. (2019). Particles are initialized at the upper boundary of the 5km thick domain with a mass flux of $F_m = 2 \cdot 10^{-5} \text{ kg s}^{-1}$ and a mean mass of the particle size distribution of $m_{m,a} = 2 \cdot 10^{-10} \text{ kg}$. The initial ice particles follow a generalized gamma distribution of particle mass with a shape parameter of 0 and a dispersion parameter of 1/3 (following Equation 9 in Khain et al. (2015)). The temperature decreases linearly from 273.1 K at $z=0 \text{ km}$ to 242.2 K at $z= 5 \text{ km}$. The supersaturation over ice is held constant at 5 % with respect to ice in the whole column and is not consumed by the growth of the particle. The simulations are performed with 250 vertical levels, which results in a vertical resolution of 20 m. The model time step is set to 5 s and the initial multiplicity is chosen to be 1000. The simulations are run for 10h, from which the last 5h are averaged in 10 min intervals to reduce noise in the analyzed profiles.

In the following, we will focus the comparison on particle number $N_m(z)$, mass flux (F_m), and mean mass $m_{m,a}$ (which is the ratio between the integrated mass density q_m and the integrated number density N).

In the first simulation experiment shown in Figure 10, we include particle properties for which the full N_m dependence is taken into account (Table 5). This setup we call hereafter the control simulation ("CTRL"). Profiles are separated into single monomers ($N_m = 1$) and aggregates ($N_m > 1$) to better distinguish the effects on what we might define as "cloud ice" and "snow" category in a bulk scheme. This separation might be important considering that there can be cases of weak aggregation. With weak aggregation, most of the particles will remain monomers and thus it is especially important to match profiles of these particles accurately.

In general, aggregation decreases the number $N_m(z)$, while the increase in the mass flux (F_m) is due to depositional growth. The mass flux of aggregates increases also due to conversion from monomers to aggregates by aggregation. The combination of both processes is causing $m_{m,a}$ to continuously increase towards the surface. Aggregation

rates in McSnow are proportional to the gravitational collection kernel (Equation 21 in Brdar and Seifert (2018)). Thus, the probability of collision for two particles is high if they have strongly different v_m and if the sum of their cross-sectional areas is large. F_N of the monomers ($N_m = 1$) decreases monotonically with decreasing height because the monomers are converted into aggregates ($N_m > 1$) by the aggregation process and there is no source of monomers like nucleation considered (Figure 10a). This decrease of F_N (and increase of f_{ma}) is especially strong at heights between 2 km to 3 km. This region of enhanced aggregation is found at heights where the temperature is close to -15 °C where the sticking efficiency has a local maximum. As a result of the conversion of monomers to aggregates F_N of the aggregates increases at heights higher than about 3.5 km (Figure 10b). At lower heights the number of aggregate-aggregate collisions outweigh the number of monomer-monomer collisions and thus the F_N of the aggregates decreases.

The signature of the conversion from monomers to aggregates is also seen in F_m of the monomers (Figure 10c). Especially in the region of enhanced aggregation, this leads to a strong decrease of F_m . In the heights above this region, depositional growth outweighs the loss of mass of the monomers to the aggregates and thus, there is an increase of F_m with decreasing height. F_m of the aggregates increases monotonously due to both depositional growth of the aggregates and conversion from monomers to aggregates (Figure 10d). In this setup, the change of F_m with height is governed by v_m and q_N at a given height. For example, a combination of low v_m and high q_N at upper layers leads to a large increase in F_m . Simply speaking, a large number of slow falling ice crystals can grow efficiently by deposition which increases F_m .

5.1 ~~in the~~

The "CTRL" simulation is now compared to simulations with a binary separation into single-monomer particles and aggregates of any monomer number larger than 1 (binary). An additional simulation is performed with no monomer number dependence (constant). Here the particle properties, that were fitted to the mean of all aggregates, are used for all particles. All simulations are done for plate and needle monomers and aggregates because we found the monomer dependence to be most pronounced for these monomer types. For the other monomer types the effect of N_m can be expected to be smaller.

The most apparent difference between the simulations with different representations of the N_m dependencies for plate monomers and aggregates of plates is the faster decrease of F_N and F_m and faster increase of $m_{m,a}$ of the monomers ($N_m = 1$) in the "constant" simulation (Figure 10). A slightly faster decrease of F_m (faster increase of $m_{m,a}$) for aggregates ($N_m > 1$) with decreasing height can be seen for both the "binary" and the "CTRL" simulation. However, all of the simulations show very similar profiles.

Figure 11 shows the same experiment as Figure 10 but using the parameterizations for needles instead of plates. Also for needles the most remarkable difference between the simulations is the difference between the "constant" and the "CTRL" run (Figure 11a and e). Also aggregate-aggregate collections are less effective in the "CTRL" run (Figure 11b and f). Note that all monomers have been depleted by aggregation at a height of about 1000 m and therefore $m_{m,a}$ is not defined below.

Overall, the differences of $m_{m,a}$ at the ground of the total ice particle population is small (factor of 1.2 and 1.4 higher $m_{m,a}$ for the "binary" and "constant" simulation for plates and factor of 0.8 lower $m_{m,a}$ for the "binary" and "constant" simulation for needles, Table 5).

Also the differences in the precipitation rates F_w are small (less than 5%; see Table 5). These small differences are due to the small difference of the absolute value of v_m at small sizes (Figure 7) and q_N at upper heights, which lead to a similar mass uptake (Figure 10). However, the precipitation rate between the "Plate CTRL" simulation and the "Needle CTRL" simulation is relatively large (Table 5), which might be due to the strongly different v_m of the monomers.

The N_m -dependency is even weaker for aggregates composed of other monomer types (Section 4.2 and 4.3). In summary, the simulation experiments with different monomer dependency indicate that a binary separation between single monomers and aggregates performs similarly well as relations which take into account a more detailed monomer dependency. Some but still small differences are found if no monomer dependency is taken into account, i.e. a single ice class for all monomer numbers is assumed. In our simulation, particles with low N_m are only prevalent at cold temperatures, where aggregation is less important due to the low sticking efficiency. Additional simulations (shown in the Supplement) with lower F_m and therefore weaker aggregation show that the "bi-

primary" simulations stay very close to the "CTRL" simulation, while the "monodep" simulations show considerably larger deviations. Hence we find that the classical separation in cloud ice (monomers) and snow (aggregates) is sufficient for the aspects of monomer number dependent particle properties.

5.2 **5.2**

In this section, we test the sensitivity of the simulations to different implementations of the $\gamma_m D_m$ formulation. In Figure 12 γ_m of plate monomers and aggregates is parameterized either as power-law or Atlas-type fit.

As we saw in Figure 9, the power-law and Atlas-type fits match very closely at small particle sizes. This explains the very close matching of the three simulations in the upper part of the simulated profiles (Figure 12) where the PSD is dominated by small particles. As soon as the aggregation becomes stronger (below ca. 3 km), in the simulations using the power law (Figure 12b) is much lower than for Atlas-type. The decreasing number flux of aggregates with lower height (Figure 12b) also indicates that especially the self-collection of aggregates is stronger than for Atlas-type. In the same height region, the mean mass of the aggregates (Figure 12f) is strongly increased for the power law (factor of 5). Instead of using an Atlas-type fit to consider the saturation of the terminal velocity, one can also think of imposing an upper limit on γ_m in the power law relation. In the "Powerlawlimit" simulation, we chose the saturation value of the Atlas-type fit (γ_{D_e}) as an upper limit. This limit does not only affect the sedimentation but all processes which depend on γ_m (e.g. aggregation). In this way, the overestimation of m_{ma} , caused by an unlimited increase of γ_m can indeed be prevented, but the height profile of F_N and m_{ma} is not as well matched as with the Atlas-type approximation. As expected, the continuously increasing γ_m in the unlimited power law leads to much stronger growth of aggregates as compared to relations which include the saturation velocity at large particle sizes. This is an interesting finding and could be one reason for the overestimation of radar reflectivities found at lower layers in ice clouds simulated with the Seifert-Beheng scheme (Heinz et al., 2017).

Although m_{ma} of the aggregates is much larger for the power law, the difference to the Atlas-type in precipitation rates is very small (smaller than 5%; Figure 12d and Table 5). Note that in more realistic cases, as e.g. in presence of stronger sublimation

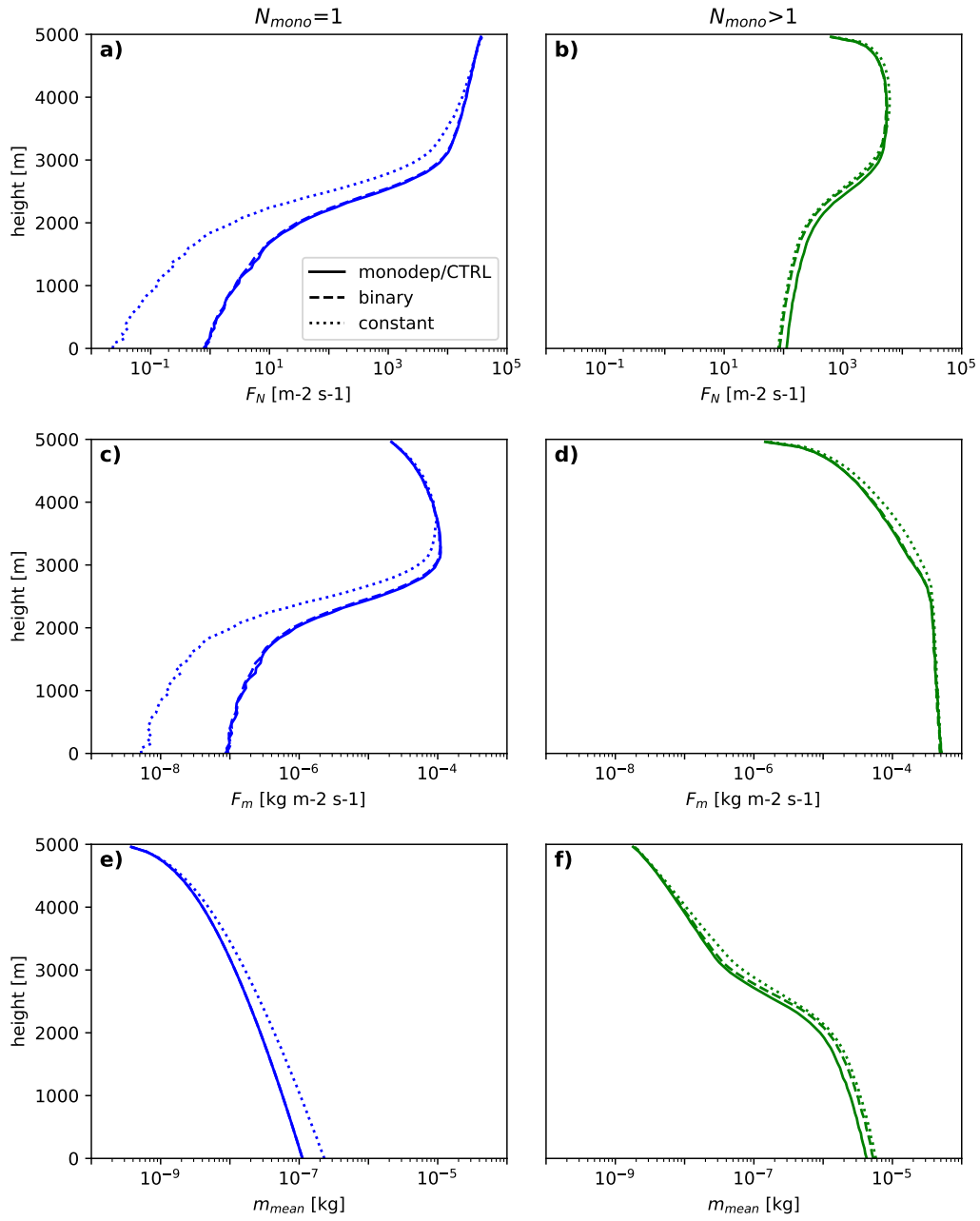
layers, the difference in m_a can induce larger differences in the precipitation rate because larger particles can fall through a thicker layer of subsaturated air before they sublimate completely.

6 **mb**

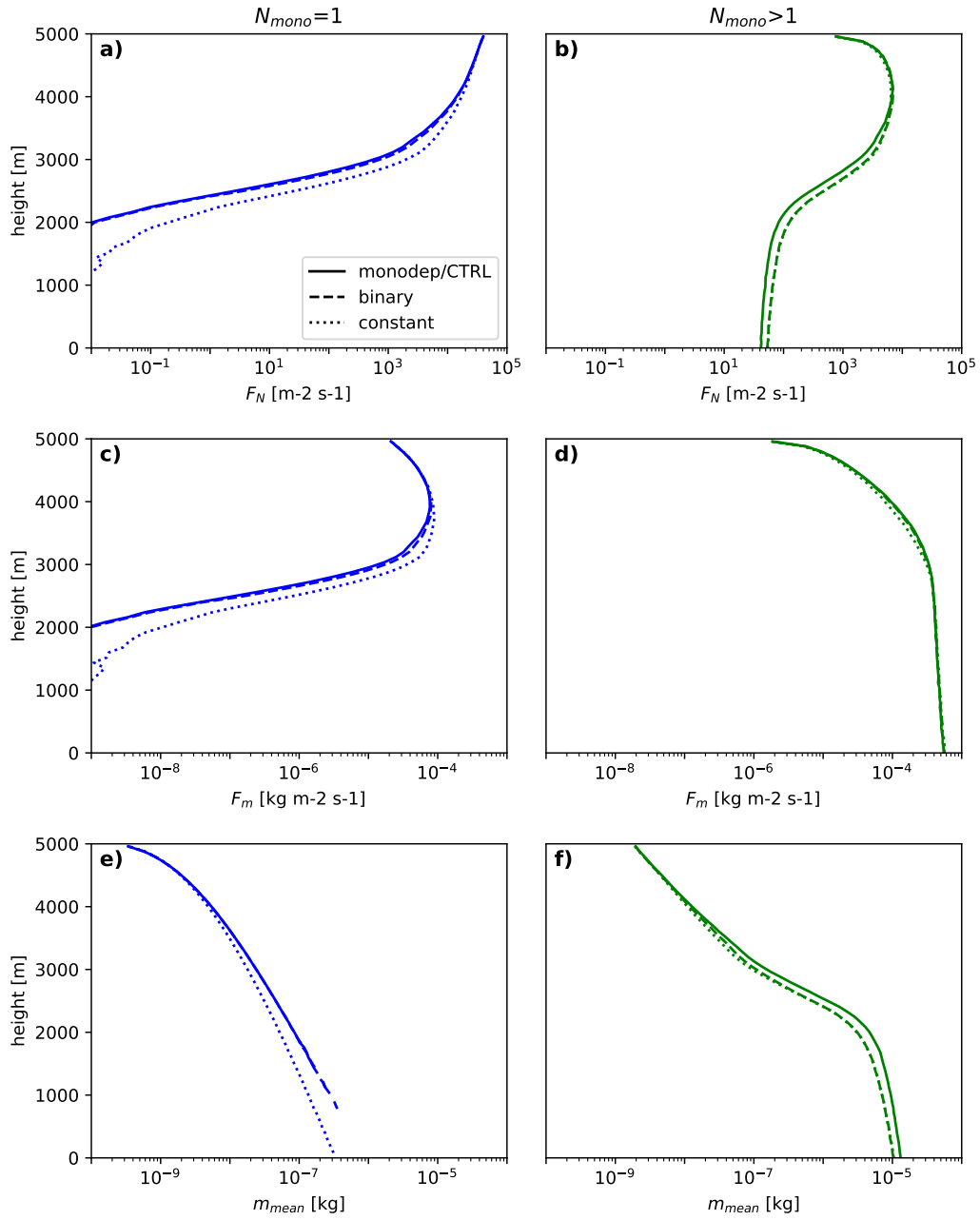
In this study, we generated a large ensemble of ice aggregates (ca. 105,000 particles) using an aggregation model and hydrodynamic theory to study the change of particle properties such as mass m , projected area A and terminal velocity v_m as a function of monomer number N_m and size. The aggregates were composed of various monomer types (plates, dendrites, needles and columns), monomer sizes and monomer numbers. In order to test the impact of habit mixtures, we also included in our analysis two different mixtures of dendrites and columns. The choice of mixing specifically dendrites and columns was motivated by in-situ observations of the composing monomers in large aggregates sampled on the ground (Lawson et al., 1998).

When comparing our aggregate properties with in-situ observations, we find A to be very similar to the results presented in Mitchell (1996) but the slope of our D_m relations is larger than the slope given in Locatelli and Hobbs (1974). A better agreement with Locatelli and Hobbs (1974) and also with theoretical considerations in Westbrook et al. (2004b) are reached for mixtures of small columns and larger dendrites (Mix2). Interestingly, this monomer mixture also achieves the best agreement with observed v_m D_m relations. Considering the large spread in the observations (Figure 3), we can overall conclude that our aggregate ensemble matches the observed range of variability and does not show any substantial bias.

Our synthetic aggregate ensemble allowed us to investigate the transition of particle properties from single crystals to aggregates with increasing number of monomers in a level of detail which is currently unavailable from in-situ observations. From A as a function of size we find the relations to change rather smoothly with increasing N_m . The differences introduced by the choice of the monomer type are found to be overall larger than due to the number of monomers. We find the exponents in the D_m and v_m D_m relations of the monomers to be closely connected to the resulting change with N_m .



$\langle \rangle$ $\langle \rangle$ $\langle \rangle$ $\langle \rangle$ $\langle N_{mono}$
 $\langle \rangle$ $\langle \rangle$ N_{mono} N_{mono} $\langle \rangle$
 $\langle \rangle$ $\langle \rangle$ $\langle \rangle$ N_{mono}
 $\langle \rangle$ $\langle \rangle$ $\langle \rangle$ $\langle \rangle$ $\langle \rangle$ v_{term} $\langle \rangle$
 $\langle \rangle$ $\langle \rangle$ F_N F_m m_{mean} $\langle \rangle$
 $\langle \rangle$ $\langle \rangle$ $\langle \rangle$ N_{mono} N_{mono} $\langle \rangle$ $\langle \rangle$



The derived A_{D_m} and m_{D_m} relations including the monomer type and number dependence were then used to calculate v_{D_m} relations. Again, we find a rather smooth transition from single crystals to aggregates rather than a ‘jump’ as found in several microphysics schemes (Figure 1b). For small sizes below a few μm , our results suggests that the ‘ice’ and ‘snow’ category of microphysics schemes should have similar properties. At larger sizes, the aggregates v_{D_m} are found to deviate more from the monomers. Again, the monomer type is found to have a larger impact than the monomer number. Aggregates of plates tend to be faster while aggregates of needles are slower than the equal-size monomer. In accordance to in-situ observations, our simulations reveal for all aggregate types a saturation of v_{D_m} at cm sizes. However, the saturation value varies for the different aggregate types from 0.8 to 1.6 m s^{-1} .

In order to potentially implement our results in microphysics schemes, we derived two-parameter power-law fits and three-parameter Atlas-type fits for single monomers ($N_m = 1$) and aggregates ($N_m > 1$) representing the commonly used ice and snow classes in models. The new power-law fits match the small sizes well and avoid unrealistic ‘jumps’ found in current schemes. However, the power laws are unable to represent the saturation of v_{D_m} at larger sizes. The Atlas-type fits are found to match the entire size range well and should thus be considered to be implemented in ice microphysics schemes as they do not substantially increase the computational costs while strongly improving the realism of the relations.

We finally tested the impact of implementing monomer dependence, habit type, and velocity fitting method on idealized aggregation simulations. For this, we used a new 1D Lagrangian Monte Carlo model which allowed us to implement the derived relations with different degree of complexity. The simulations experiments revealed that there is only a very small impact of using a relation of only two monomer categories (single particle and aggregate) as compared to a continuous monomer number dependence. A single category which does not take any monomer number into account shows slightly larger deviations but the variability due to monomer type is in general larger than the impact of monomer number.

In a second simulation experiment, we investigated the impact of using a power law or an Atlas-type fit for v_{D_m} . The simulations show very small differences in the upper part of the cloud where the profiles are dominated by small particles which are fitted sim-

ilarly well with the two relations. Once aggregation becomes more dominant and the spread of particle sizes shifts to larger sizes, the simulations using the power law lead to a much stronger aggregation and in particular stronger self-aggregation of particles as compared to the Atlas-type fit. The impact of the widely used power-law relations for v_m should thus be further studied for bulk schemes as it seems to be likely that they might cause an overestimation of aggregation and snow particle sizes.

We also shortly investigated the sensitivity of our derived relations to particle tumbling and the choice of the hydrodynamic theory. While tumbling can significantly affect the properties of single monomers, it has a surprisingly small effect on our results for the aggregates. The choice of the hydrodynamic theory is a larger source of uncertainty which should be further investigated in future studies. It seems to be important in the future to better constraint the composition of aggregates regarding the monomer type. This question could be approached by improved in-situ techniques but also with detailed models that allow to predict the particle habit such as presented in e.g. Woods et al. (2007); Jensen et al. (2017); Shima et al. (2019).

AAA

A ~~isa~~

The terminal velocity v_m of the simulated aggregates from this study is compared to recent observations of falling ice particle properties and frequently used literature in Section 3.2. These surface observations are from the Centre for Atmospheric Research Experiments (CARE), Canada. It is a research facility of the Air Quality Research Branch of the Meteorological Service of Canada, located about 80 km north of Toronto, Ontario (lat = 44° 13' 58" N, lon = 79° 46' 53" W). The instrumentation includes a video-disdrometer, Particle Imaging Package (PIP), precipitation weighing gauge, and meteorological measurements of e.g. wind velocity.

More detail about PIP can be found in von Lerber et al. (2017) and references therein. The particle sizes are recorded in the range of 0.2 - 26 mm (disk equivalent diameter) with a resolution of 0.2 mm, which is converted to the side projected $D_{m,s}$. In practice, the minimum reliable size with measurement of v_m is approximately 0.5 mm. Observations of the side projected maximum dimension $D_{m,s}$ can be conducted from the gray-scale video images. The velocity v_m is obtained from the observations of the con-

secutive frames. The observed v_m utilized in the Figures 1a and 3c-d are separated from the whole dataset by limiting the exponent of the "5-minute m-D relation" between 1.7-2.2 to exclude rimed particles (von Lerber et al., 2017). To apply this m-D threshold, the mass of the single particle and D_{nw} has to be retrieved. The mass estimate of a single particle is calculated from the observed v_m corrected D_{nw} and area ratio using different parametrizations of the hydrodynamic theory (Bhm, 1989; Mitchell & Heymsfield, 2005; Heymsfield & Westbrook, 2010). For each snowfall event, each of these parameterizations are calculated and the one which minimizes the error in the estimate of the liquid water equivalent precipitation with respect to the precipitation gauge is selected for that event. This procedure and the related uncertainties are described more in detail in von Lerber et al. (2017). Additionally observations during 5-minutes intervals, where the mean horizontal wind speed exceeds 4 m s^{-1} are excluded to reduce turbulence effects (similar to Brandes et al. (2008)).

After applying these filters, the dataset, which covers the winters from 2014 to 2017 with 48 snowfall events, contains about 4.3 million ice particles. It should be noted that PIP is providing a measurement of the ensemble of particles and no particle by particle-based classification is performed. Hence, the measurement volume includes mixtures of different habits.

A.1.1.1

A.1.1.1

A.1.1.1

As mentioned in Section 2.2, the hydrodynamic models of B92, KC05 and HW10 differ in several aspects. The $\text{Re}(X)$ relation requires assumptions about particle surface roughness, which are differently implemented in the models. Also the definition of X is different (Table A1). While in B92 X is proportional to $m D_{nw}^{0.5} A^{-0.5}$, X is proportional to $m D_{nw} A^{-0.5}$ in HW10 and $m D_{nw}^2 A^{-1}$ in KC05. As a result in B92 and HW10, v_m increases slower with decreasing area ratio ($A = 4A^{-1}D^{-2}$) than in the formulation of KC05. The empirical correction α due to wake turbulence is also applied in KC05 but not in HW10.

These differences affect the behaviour of v_m at large sizes and the monomer number dependency (which we quantify by β_m). Without the empirical correction of

	B92	HW10	KC05
X	$mD_{nu}^{0.5} A^{-0.5}$	$mD_{nu} A^{-0.5}$	$mD_{nu}^2 A$
$v_m < 1$	$D_{nu}^{m-0.5} A^{-0.5}$	$D_{nu}^{m-0.5} A$	D_{nu}^{m-A+1}
$v_m > 1$	$D_{nu}^{m-0.5} A^{-1.5} 0.5$	$D_{nu}^{m-0.5} A^{-1} 0.5$	$D_{nu}^{m-A} 0.5$
$s_m =$	$b_{m,agg} b_{m,1}$	$b_{m,agg} b_{m,1}$	$b_{m,agg} b_{m,1}$
	$0.25(b_{A,agg} b_{A,1})$	$0.5(b_{A,agg} b_{A,1})$	$(b_{A,agg} b_{A,1})$

X (which considers wake turbulence) only saturates if $v_m > 1$. For example with HW10 the saturation would be reached for $0.5b_{A,1} = 0$ (Table A1). This is e.g. not the case for aggregates of plates simulated in this study and therefore HW10 does not predict a saturation of v_m at larger sizes (Figure A1a).

Also the sign and the strength of the increase/decrease of v_m with increasing N_m depends on the formulation of X . In Section 4.3 we introduced s_m as a measure for this monomer number dependency. Applying this measure to the aggregates of plates yields $s_m = 0.21$ for HW10 and $s_m = 0.06$ for KC05. Both HW10 and KC05 show the decrease of v_m with increasing N_m which we saw when using B92, but this decrease is very weak for KC05.

2.5

To investigate the effect of the tumbling of the aggregates (as reported e.g. by Garrett and Yuter (2014a)) on the projected area A and v_m the particles are tilted with a standard deviation of 0, 20, 40 and 60, around the principal axis (Figure A2). This is done only after the final aggregate is assembled and thereby does not influence the structure of the aggregates. This rotation reduces A and in turn, v_m increases.

Figure A1. Same as Figure 7a (aggregates of plates) but using HW10 in a) and KC05 in b)

858 The monomers (top panel in Figure A2) are stronger affected by tumbling (espe-
 859 cially at large D_{\max}) due to their lower aspect ratio (not shown). The largest increase
 860 in v_{term} with increasing tumbling is found for KC05 due to the largest increase in the
 861 Best number with decreasing A (see Section 2.2). B92 shows the least influence of tum-
 862 bling, which increases v_{term} at maximum by about 0.1 m s^{-1} and has a negligible effect
 863 on v_{term} for the aggregates.

864 A3 Mean Absolute Error of the Mass and Area-Size Relations

865 In Sections 4.2 and 4.4, we provided fit relations for mass and area with and with-
 866 out taking into account the monomer number dependency of the simulated aggregates.
 867 The mean absolute error of the fits shown in Table 3 and Table 4 (normalized by the prop-
 868 erties of the monomers; e.g. shown for plates with the green dotted lines in Figure 5) is
 869 shown in Table A2

870 Acknowledgments

871 Contributions by M.K., S.K. and D.O. were funded by the German Research Founda-
 872 tion (DFG) under grant KN 1112/2-1 as part of the Emmy-Noether Group Optimal com-
 873 bination of Polarimetric and Triple Frequency radar techniques for Improving Microphys-
 874 ical process understanding of cold clouds (OPTIMIce). A.v.L. gratefully acknowledges
 875 the funding by the Deutsche Forschungsgemeinschaft (DFG, German Research Founda-
 876 tion) Project-ID 268020496 TRR 172, within the Transregional Collaborative Research

- Bernauer, F., Hrkamp, K., Rhm, W., & Tschiersch, J. (2016, may). Snow event classification with a 2D video disdrometer - A decision tree approach. *Journal of Applied Meteorology and Climatology*, 55(5), 1861-1875. doi: 10.1016/j.atmosres.2016.01.001
- Rhm, J. (1989). *Aggregation of ice crystals* (Vol. 46) (No. 15). Retrieved from [http://journals.ametsoc.org/doi/abs/10.1175/1520-0469\(1989\)028<1904:AGEFTT2.0.CO;2](http://journals.ametsoc.org/doi/abs/10.1175/1520-0469(1989)028<1904:AGEFTT2.0.CO;2) doi: 10.1175/1520-0469(1989)028<1904:AGEFTT2.0.CO;2
- Rhm, J. (1992). A general hydrodynamic theory for mixed-phase microphysics. Part I: Drag and fall speed of hydrometeors. *Journal of Applied Meteorology and Climatology*, 31(4), 253-274.
- Brandes, E. A., Ikeda, K., Thompson, G., & Schönhuber, M. (2008, oct). Aggregate terminal velocity/temperature relations. *Journal of Applied Meteorology and Climatology*, 47(10), 2729-2736. Retrieved from <http://journals.ametsoc.org/doi/abs/10.1175/2008JAMC1869.1> doi: 10.1175/2008JAMC1869.1
- Brdar, S., & Seifert, A. (2018). McSnow: A Monte-Carlo Particle Model for Riming and Aggregation of Ice Particles in a Multidimensional Microphysical Phase Space. *Monthly Weather Review*, 146(1), 187-206. doi: 10.1002/2017MS001167
- Brown, S. R. (1970). *Snowfall* (Tech. Rep.). Fort Collins, Colorado: Department of Atmospheric Science Colorado State University.
- Bergesser, R. E., Giovacchini, J. P., & Castellano, N. E. (2019, oct). Sedimentation analysis of columnar ice crystals in viscous flow regimes. *Journal of Applied Meteorology and Climatology*, 58(10), 3684-3694. Retrieved from <https://onlinelibrary.wiley.com/doi/abs/10.1002/qj.3684> doi: 10.1002/qj.3684
- Connolly, P. J., Emersic, C., & Field, P. R. (2012). A laboratory investigation into the aggregation efficiency of small ice crystals. *Journal of Applied Meteorology and Climatology*, 51(4), 2055-2076. doi: 10.5194/acp-12-2055-2012
- Cornford, S. G. (1965, jan). Fall speeds of precipitation elements. *Journal of Applied Meteorology and Climatology*, 4(1), 91-94. Retrieved from <http://doi.wiley.com/10.1002/qj.49709138713> doi: 10.1002/qj.49709138713
- Dunnavan, E. L., Jiang, Z., Harrington, J. Y., Verlinde, J., Fitch, K., & Garrett,

- T. J. (2019, dec). The Shape and Density Evolution of Snow Aggregates. *JAMES*, 7(12), 3919-3940. Retrieved from <http://journals.ametsoc.org/doi/10.1175/JAS-D-19-0066.1> doi: 10.1175/JAS-D-19-0066.1
- Frick, C., Seifert, A., & Wernli, H. (2013). A bulk parametrization of melting snow flakes with explicit liquid water fraction for the COSMO model. *JAMES*, 6(6), 1925-1939. doi: 10.5194/gmd-6-1925-2013
- Garrett, T. J., Fallgatter, C., Shkurko, K., & Howlett, D. (2012, nov). Fall speed measurement and high-resolution multi-angle photography of hydrometeors in free fall. *JAMES*, 5(11), 2625-2633. Retrieved from <http://www.atmos-meas-tech.net/5/2625/2012/> doi: 10.5194/amt-5-2625-2012
- Garrett, T. J., & Yuter, S. E. (2014a). Observed influence of riming, temperature, and turbulence on the fallspeed of solid precipitation. *JAMES*, 4(18), 6515-6522. doi: 10.1002/2014GL061016
- Garrett, T. J., & Yuter, S. E. (2014b, sep). Observed influence of riming, temperature, and turbulence on the fallspeed of solid precipitation. *JAMES*, 4(18), 6515-6522. Retrieved from <http://doi.wiley.com/10.1002/2014GL061016> doi: 10.1002/2014GL061016
- Hashino, T., Cheng, K. Y., Chueh, C. C., & Wang, P. K. (2016, may). Numerical study of motion and stability of falling columnar crystals. *JAMES*, 3(5), 1923-1942. Retrieved from <http://journals.ametsoc.org/doi/10.1175/JAS-D-15-0219.1> doi: 10.1175/JAS-D-15-0219.1
- Hashino, T., & Tripoli, G. J. (2011). The Spectral Ice Habit Prediction System (SHIPS). Part IV: Box model simulations of the habit-dependent aggregation process. *JAMES*, 6(6), 1142-1161. Retrieved from <http://journals.ametsoc.org/doi/abs/10.1175/2011JAS3667.1> doi: 10.1175/2011JAS3667.1
- Heinz, R., Dipankar, A., Henken, C. C., Moseley, C., Sourdeval, O., Tomel, S., ... Quaas, J. (2017). Large-eddy simulations over Germany using ICON: a comprehensive evaluation. *JAMES*, 3(702), 691-700. doi: 10.1002/qj.2947

- Heymseld, A. J. (1972, oct). Ice Crystal Terminal Velocities. *Journal of Atmospheric Sciences*, 29(7), 1348-1357. doi: 10.1175/1520-0469(1972)029<1348:ictvi2.0.co;2
- Heymseld, A. J., & Westbrook, C. D. (2010). Advances in the estimation of ice particle fall speeds using laboratory and field measurements. *Journal of Atmospheric Sciences*, 67(8), 2469-2482. Retrieved from <http://journals.ametsoc.org/doi/abs/10.1175/2010JAS3379>. doi: 10.1175/2010JAS3379.1
- Jakob, C. (2002). Ice clouds in numerical weather prediction models - Progress, problems and prospects. *Journal of Atmospheric Sciences*, 59(3), 327-345. Retrieved from https://books.google.de/books?hl=de&lr=&id=581fg4xeo8C&oi=fnd&pg=PA327&dq=Ice+clouds+in+numerical+weather+prediction+models:+progress,+problems,+and+prospects&ots=U_sX_M3vL&sig=1vBgpvEDsydOCRJHHH-FeH5cHc
- Jensen, A. A., Harrington, J. Y., Morrison, H., & Milbrandt, J. A. (2017, jun). Predicting ice shape evolution in a bulk microphysics model. *Journal of Atmospheric Sciences*, 74(6), 2081-2104. Retrieved from <http://journals.ametsoc.org/doi/10.1175/JAS-D-16-0350>. doi: 10.1175/JAS-D-16-0350.1
- Jiang, Z., Verlinde, J., Clothiaux, E. E., Aydin, K., & Schmitt, C. (2019, jul). Shapes and Fall Orientations of Ice Particle Aggregates. *Journal of Atmospheric Sciences*, 76(7), 1903-1916. Retrieved from <http://journals.ametsoc.org/doi/10.1175/JAS-D-18-0251>. doi: 10.1175/JAS-D-18-0251.1
- Kajikawa, M. (1972). Measurement of Falling Velocity of Individual Snow Crystals. *Journal of Atmospheric Sciences*, 29(6), 577-584. Retrieved from [https://www.jstage.jst.go.jp/article/jmsj1965/50/6/50\(6\)_577](https://www.jstage.jst.go.jp/article/jmsj1965/50/6/50(6)_577). doi: 10.2151/jmsj1965.50.577
- Khain, A. P., Beheng, K. D., Heymseld, A. J., Korolev, A., Krichak, S. O., Levin, Z., ... Yano, J. I. (2015). Representation of microphysical processes in cloud-resolving models: Spectral (bin) microphysics versus bulk parameterization. *Journal of Atmospheric Sciences*, 72(2), 247-262. doi: 10.1002/2014RG000468
- Khvorostyanov, V. I., & Curry, J. A. (2005). Fall velocities of hydrometeors in the

- atmosphere: Revisions to a continuous analytical power law
 , 8 (12), 4343-4357. doi: 10.1175/JAS3622.1
- Kruger, A., & Krajewski, W. F. (2002, may). Two-dimensional video disdrometer:
 A description. *Journal of Applied Meteorology*, 41(5), 602-
 617. Retrieved from [http://journals.ametsoc.org/doi/abs/10.1175/1520-0426\(2002\)041<0602:TDVDAD2.0.CO;2](http://journals.ametsoc.org/doi/abs/10.1175/1520-0426(2002)041<0602:TDVDAD2.0.CO;2)
 doi: 10.1175/1520-0426(2002)041<0602:TDVDAD2.0.CO;2
- Langleben, M. P. (1954). The terminal velocity of snow flakes. *Journal of Applied Meteorology*, 13(344), 174-181. doi: 10.1002/qj.49708034404
- Lawson, R. P., Stewart, R. E., & Angus, L. J. (1998). Observations and numerical simulations of the origin and development of very large snow flakes. *Journal of Applied Meteorology*, 37(21), 3209-3229. doi: 10.1175/1520-0469(1998)037<3209:OANSOT2.0.CO;2
- Leinonen, J., Kneifel, S., & Hogan, R. J. (2018). Evaluation of the Rayleigh-Gans approximation for microwave scattering by rimed snow flakes. *Journal of Applied Meteorology*, 57(4), 778-788. doi: 10.1002/qj.3093
- Leinonen, J., & Moisseev, D. (2015). What do triple-frequency radar signatures reveal about aggregate snow flakes? *Journal of Applied Meteorology*, 54(1), 229-239. doi: 10.1002/2014JD022072
- Leinonen, J., & Syrmer, W. (2015, aug). Radar signatures of snow flake rimming: A modeling study. *Journal of Applied Meteorology*, 54(8), 346-358. Retrieved from <http://doi.wiley.com/10.1002/2015EA000102> doi: 10.1002/2015EA000102
- Locatelli, J. D., & Hobbs, P. V. (1974). Fall speeds and masses of solid precipitation particles. *Journal of Applied Meteorology*, 13(15), 2185-2197. Retrieved from <http://doi.wiley.com/10.1029/JC079i015p02185> doi: 10.1029/jc079i015p02185
- Mitchell, D. L. (1996, jun). Use of mass- and area-dimensional power laws for determining precipitation particle terminal velocities. *Journal of Applied Meteorology*, 35(12), 1710-1723. Retrieved from [http://journals.ametsoc.org/doi/abs/10.1175/1520-0469\(1996\)035<1710:BAUOMAAD2.0.CO;2](http://journals.ametsoc.org/doi/abs/10.1175/1520-0469(1996)035<1710:BAUOMAAD2.0.CO;2) doi: 10.1175/1520-0469(1996)035<1710:

UOMAAD2.0.CO;2

- Mitchell, D. L., & Heymsfield, A. J. (2005). Revisions in the treatment of ice particle terminal velocities, highlighting aggregates. *Journal of Climate*, 18(5), 1637–1644. Retrieved from <http://adsabs.harvard.edu/abs/2005JAtS...42.1637M> <http://journal.ametsoc.org/doi/pdf/10.1175/JAS413>. doi: 10.1175/JAS413
- Morales, A., Posselt, D. J., Morrison, H., & He, F. (2019). Assessing the influence of microphysical and environmental parameter perturbations on orographic precipitation. *Journal of Climate*, 32(5), 1373–1395. doi: 10.1175/JAS-D-18-0301.1
- Morrison, H., Curry, J. A., & Khvorostyanov, V. I. (2005). A new double-moment microphysics parameterization for application in cloud and climate models. Part I: Description. *Journal of Climate*, 18(6), 1665–1677. Retrieved from <http://journal.ametsoc.org/doi/abs/10.1175/JAS446>. doi: 10.1175/JAS446.1
- Morrison, H., & Milbrandt, J. A. (2015, jan). Parameterization of cloud microphysics based on the prediction of bulk ice particle properties. Part I: Scheme description and idealized tests. *Journal of Climate*, 28(1), 287–311. Retrieved from <http://journal.ametsoc.org/doi/10.1175/JAS-D-14-0065>. doi: 10.1175/JAS-D-14-0065.1
- Nakaya, U., & Terada, T. J. (1935, jan). Simultaneous Observations of the Mass, Falling Velocity and Form of Individual Snow Crystals. *Journal of Geophysical Research*, 40(7), 191–200.
- Nettesheim, J. J., & Wang, P. K. (2018). A numerical study on the aerodynamics of freely falling planar Ice Crystals. *Journal of Climate*, 31(9), 2849–2865. doi: 10.1175/JAS-D-18-0041.1
- Newman, A. J., Kucera, P. A., & Bliven, L. F. (2009, feb). Presenting the Snowflake Video Imager (SVI). *Journal of Applied Meteorology and Climatology*, 48(2), 167–179. Retrieved from <http://journal.ametsoc.org/doi/abs/10.1175/2008JTECHA1148>. doi: 10.1175/2008JTECHA1148.1
- Ori, D., Maestri, T., Rizzi, R., Cimini, D., Montopoli, M., & Marano, F. S. (2014, aug). Scattering properties of modeled complex snowflakes and mixed-phase particles at microwave and millimeter frequencies. *Journal of Applied Meteorology and Climatology*, 53(16), 993–9947. Retrieved from <http://doi.wiley>

- . com/10.1002/2014JD021616 doi:10.1002/2014JD021616
- Pruppacher, H. R., & Klett, J. D. (1998). Microphysics of Clouds and Precipitation. *Journal of Atmospheric Sciences*, 55(4), 381-382. doi: 10.1080/02786829808965531
- Prybylo, V. M., Sulia, K. J., Schmitt, C. G., Lebo, Z. J., & May, W. C. (2019). The ice Particle and Aggregate Simulator (IPAS). Part I: Extracting dimensional properties of ice-ice aggregates for microphysical parameterization. *Journal of Atmospheric Sciences*, 76(6), 1661-1676. Retrieved from <http://journals.ametsoc.org/doi/10.1175/JAS-D-18-0187.1> doi: 10.1175/JAS-D-18-0187.1
- Sanderson, B. M., Piani, C., Ingram, W. J., Stone, D. A., & Allen, M. R. (2008, feb). Towards constraining climate sensitivity by linear analysis of feedback patterns in thousands of perturbed-physics GCM simulations. *Journal of Climate*, 21(2-3), 175-190. Retrieved from <http://link.springer.com/10.1007/s00382-007-0280-7> doi: 10.1007/s00382-007-0280-7
- Schmidt, G. A., Bader, D., Donner, L. J., Elsaesser, G. S., Golaz, J. C., Hannay, C., ... Saha, S. (2017, sep). Practice and philosophy of climate model tuning across six US modeling centers. *Journal of Geophysical Research*, 122(9), 3207-3223. Retrieved from <https://www.geosci-model-dev.net/10/3207/2017/> doi: 10.5194/gmd-10-3207-2017
- Schmitt, C. G., & Heymseld, A. J. (2010, may). The dimensional characteristics of ice crystal aggregates from fractal geometry. *Journal of Atmospheric Sciences*, 67(5), 1605-1616. Retrieved from <http://journals.ametsoc.org/doi/abs/10.1175/2009JAS3187> doi: 10.1175/2009JAS3187.1
- Schmitt, C. G., Sulia, K. J., Lebo, Z. J., Heymseld, A. J., Prybylo, V., & Connolly, P. (2019, aug). The Fall Speed Variability of Similarly Sized Ice Particle Aggregates. *Journal of Atmospheric Sciences*, 76(8), 1751-1761. Retrieved from <http://journals.ametsoc.org/doi/10.1175/JAMC-D-18-0291.1> doi: 10.1175/JAMC-D-18-0291.1
- Seifert, A., & Beheng, K. D. (2006). A two-moment cloud microphysics parameterization for mixed-phase clouds. Part 1: Model description. *Journal of Atmospheric Sciences*, 63(1-2), 45-66. doi: 10.1007/s00703-005-0112-4
- Seifert, A., Blahak, U., & Buhr, R. (2014). On the analytic approximation of bulk

- collision rates of non-spherical hydrometeors. *Atmospheric Chemistry and Physics*, 7(2), 463–478. doi: 10.5194/gmd-7-463-2014
- Seifert, A., Leinonen, J., Siewert, C., & Kneifel, S. (2019, mar). The Geometry of Rimed Aggregate Snowflakes: A Modeling Study. *Atmospheric Chemistry and Physics*, 19(3), 7127–7131. doi: 10.1029/2018MS001519
- Shima, S.-i., Kusano, K., Kawano, A., Sugiyama, T., & Kawahara, S. (2009). The super-droplet method for the numerical simulation of clouds and precipitation: A particle-based and probabilistic microphysics model coupled with a non-hydrostatic model. *Journal of Geophysical Research*, 114(D62), 13071–13080. doi: 10.1002/qj.441
- Shima, S.-i., Sato, Y., Hashimoto, A., & Ryohei Misumi. (2019). GMDD - Predicting the morphology of ice particles in deep convection using the super-droplet method: development and evaluation of SCALE-SDM 0.2.5-2.2.0/2.2.1. *Geoscientific Model Development Discussions*. Retrieved from <https://www.geoscientific-model-development-discussions.net/gmd-2019-294/>
- Syrmer, W., & Zawadzki, I. (2010, oct). Snow studies. Part II: Average relationship between mass of snowflakes and their terminal fall velocity. *Journal of Applied Meteorology and Climatology*, 49(10), 3319–3335. Retrieved from <https://journals.ametsoc.org/doi/abs/10.1175/2010JAS3330> doi: 10.1175/2010JAS3390.1
- Tiira, J., Moisseev, D. N., Von Lerber, A., Ori, D., Tokay, A., Bliven, L. F., & Petersen, W. A. (2016, sep). Ensemble mean density and its connection to other microphysical properties of falling snow as observed in Southern Finland. *Atmospheric and Environmental Technology*, 9(9), 4825–4841. Retrieved from <https://www.atmos-meas-tech.net/9/4825/2016/> doi: 10.5194/amt-9-4825-2016
- Tsai, T.-C., & Chen, J.-P. (2020, mar). Multi-Moment Ice Bulk Microphysics Scheme with Consideration for Particle Shape and Apparent Density. Part I: Methodology and Idealized Simulation. *Journal of Geophysical Research*. doi: 10.1175/jas-d-19-0125.1
- von Lerber, A., Moisseev, D., Bliven, L. F., Petersen, W. A., Harri, A. M., & Chandrasekar, V. (2017). Microphysical properties of snow and their link to Ze-S relations during BAECC 2014. *Atmospheric Chemistry and Physics*

- 1140 ogy, 56(6), 1561{1582. doi: 10.1175/JAMC-D-16-0379.1
- 1141 Westbrook, C. D., Ball, R. C., Field, P. R., & Heyms eld, A. J. (2004a, aug). The-
1142 ory of growth by di erential sedimentation, with application to snow ake for-
1143 mation. Physical Review E - Statistical Physics, Plasmas, Fluids, and Related
1144 Interdisciplinary Topics , 70(2), 7. Retrieved from [https://link.aps.org/](https://link.aps.org/doi/10.1103/PhysRevE.70.021403)
1145 doi/10.1103/PhysRevE.70.021403 doi: 10.1103/PhysRevE.70.021403
- 1146 Westbrook, C. D., Ball, R. C., Field, P. R., & Heyms eld, A. J. (2004b). Univer-
1147 sality in snow ake aggregation. Geophysical Research Letters31(15). doi: 10
1148 .1029/2004GL020363
- 1149 Westbrook, C. D., & Sephton, E. K. (2017). Using 3-D-printed analogues to inves-
1150 tigate the fall speeds and orientations of complex ice particles.Geophysical Re-
1151 search Letters, 44(15), 7994{8001. doi: 10.1002/2017GL074130
- 1152 Woods, C. P., Stoelinga, M. T., & Locatelli, J. D. (2007, nov). The IMPROVE-1
1153 storm of 1-2 February 2001. Part III: Sensitivity of a mesoscale model sim-
1154 ulation to the representation of snow particle types and testing of a bulk
1155 microphysical scheme with snow habit prediction. Journal of the Atmospheric
1156 Sciences 64(11), 3927{3948. Retrieved from[http://journals.ametsoc.org/](http://journals.ametsoc.org/doi/abs/10.1175/2007JAS2239.1)
1157 doi/abs/10.1175/2007JAS2239.1 doi: 10.1175/2007JAS2239.1
- 1158 Zawadzki, I., Jung, E., & Lee, G. (2010, may). Snow studies. Part I: A study of nat-
1159 ural variability of snow terminal velocity. Journal of the Atmospheric Sciences
1160 67(5), 1591{1604. Retrieved from[http://journals.ametsoc.org/doi/abs/](http://journals.ametsoc.org/doi/abs/10.1175/2010JAS3342.1)
1161 10.1175/2010JAS3342.1 doi: 10.1175/2010JAS3342.1
- 1162 Zikmunda, J., & Vali, G. (1972, oct). Fall Patterns and Fall Velocities of Rimed
1163 Ice Crystals. Journal of the Atmospheric Sciences 29(7), 1334{1347. doi: 10
1164 .1175/1520-0469(1972)029<1334:fpafov>2.0.co;2

Supporting Information for "Ice Particle Properties Inferred from Aggregation Modelling"

M. Karrer¹, A. Seifert², C. Siewert², D. Ori¹, A. von Lerber^{1,3}, S. Kneifel¹

¹Institute for Geophysics and Meteorology, University of Cologne, Cologne, Germany

²Deutscher Wetterdienst, Offenbach, Germany

³Finnish Meteorological Institute, Helsinki, Finland

Contents of this file

1. Figures S1 to S17

Introduction

In this supplemental material we provide additional figures, which may be interesting for some readers but are not necessary to draw the conclusions of the main text. We show figures with the same or similar content than figures in the main text, but using a different size definition or additional monomer types or additional simulations or additional variables supplementary to the simulations with McSnow.

Particle Properties Against Mass Equivalent Diameter

Figure S1 shows the same plot as Figure 7 but using the mass-equivalent diameter D_{eq} . This depiction might be helpful in applications where m is the primary variable (instead of D_{max}). Overall Figure 7 and Figure S1 look similar and we do not observe systematic shifts in the dependency of v_{term} on N_{mono} when changing the variable.

Dependence of Aggregate Mass, Area and Terminal Velocity on Monomer Number for Additional Monomer Types

Figures S2 and S5 show the particle properties m and A and Figure S3 and S5 show v_{term} of dendrites and columns. While dendrites behave similarly to plates (both are planar-like shapes), columns behave similarly to needles (both are column-like shapes). For dendrites m , A and v_{term} is decreasing with increasing N_{mono} . For columns m , A and v_{term} is increasing with increasing N_{mono} .

Power Law and Atlas-type Fits for Terminal Velocity for Additional Monomer Types

Figures S6 to S10 show power law and Atlas-type fits for monomers and aggregates for needles, dendrites, columns as well as the mixture of columns and dendrites ("Mix1" and "Mix2"). For the mixtures "Mix1" and "Mix2" the properties of particles with $N_{mono} = 1$ are defined by the properties of the column monomer. Also for these habits, the Atlas-type fit allows a much more accurate representation of v_{term} at large sizes. The deviation between the assumptions in the microphysics schemes and the dendrites is especially large. The monomers and aggregates of columns and "Mix2" (which assume monomers with $D_{max} < 1mm$ to be columns and monomers with $D_{max} > 1mm$ to be dendrites) exhibit larger values of v_{term} which is closer to the assumptions in the microphysics schemes. "Mix2" (here the selection of the monomer type - dendrite or column - is random) shows a large spread of v_{term} of the individual particles.

Additional Simulations with the Lagrangian Particle Mode McSnow

Figures S11 to S13 show McSnow simulations testing the impact of the representation of the monomer number dependency analog to Figure 10 but with a lower mass flux F_m at the initialization height (model top).

In the simulations beginning with a two times up to a ten times lower F_m (Figure S14 to S17) the mean and median number of monomers is increasingly smaller. As a result, also the height range where more than half of the particles are monomers is larger. In the simulation shown in Figure S13 the median of N_{mono} stays at one for all heights of the simulation. This prevalence of the monomers deteriorates the accuracy of the simulation where the particle properties of all particles are approximated by a single relation (“constant”). However the “binary” simulation (where monomers have distinct particle properties) deviates even less from the “CTRL” simulation compared to the simulation with the higher F_m , which is shown in Figure 10.

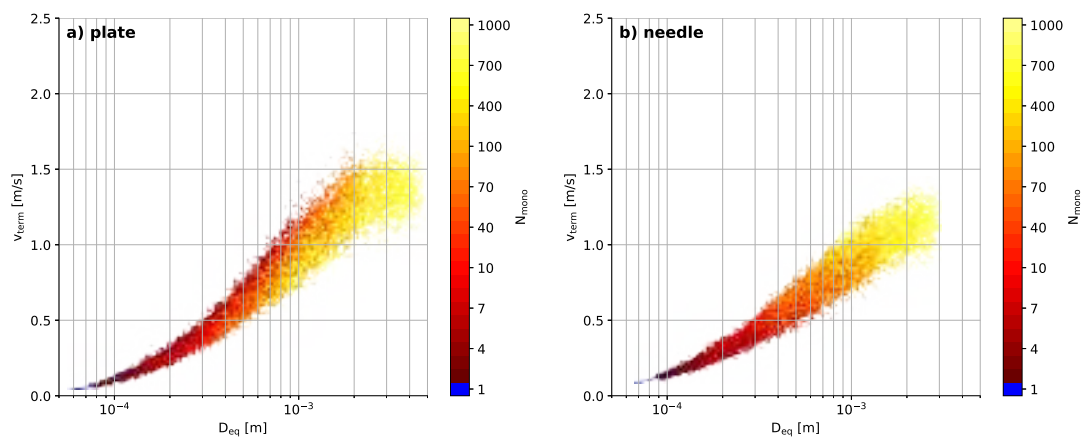


Figure S1. Same as Figure 7 but using the mass-equivalent diameter D_{eq} . Fits for different values of N_{mono} have not been calculated.

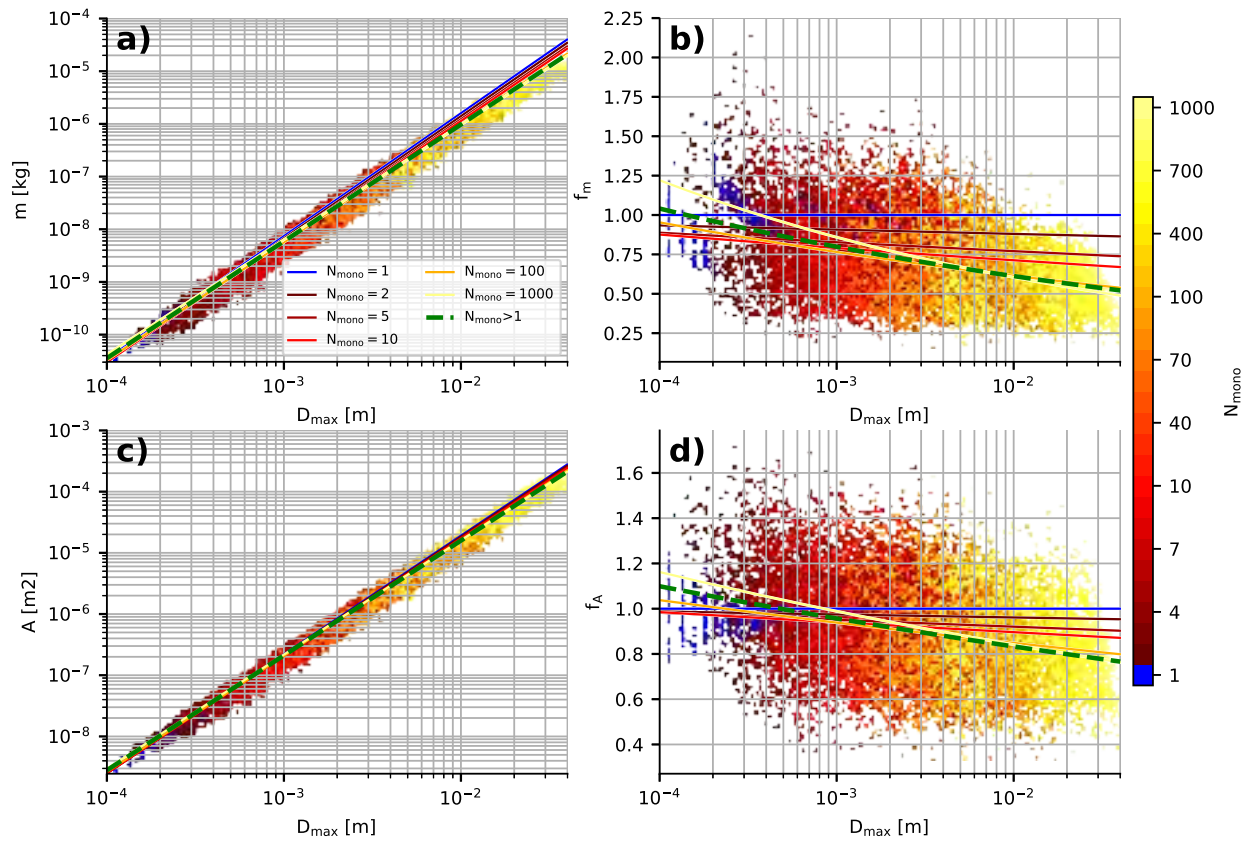


Figure S2. Same as Figure 6 but for aggregates of dendrites

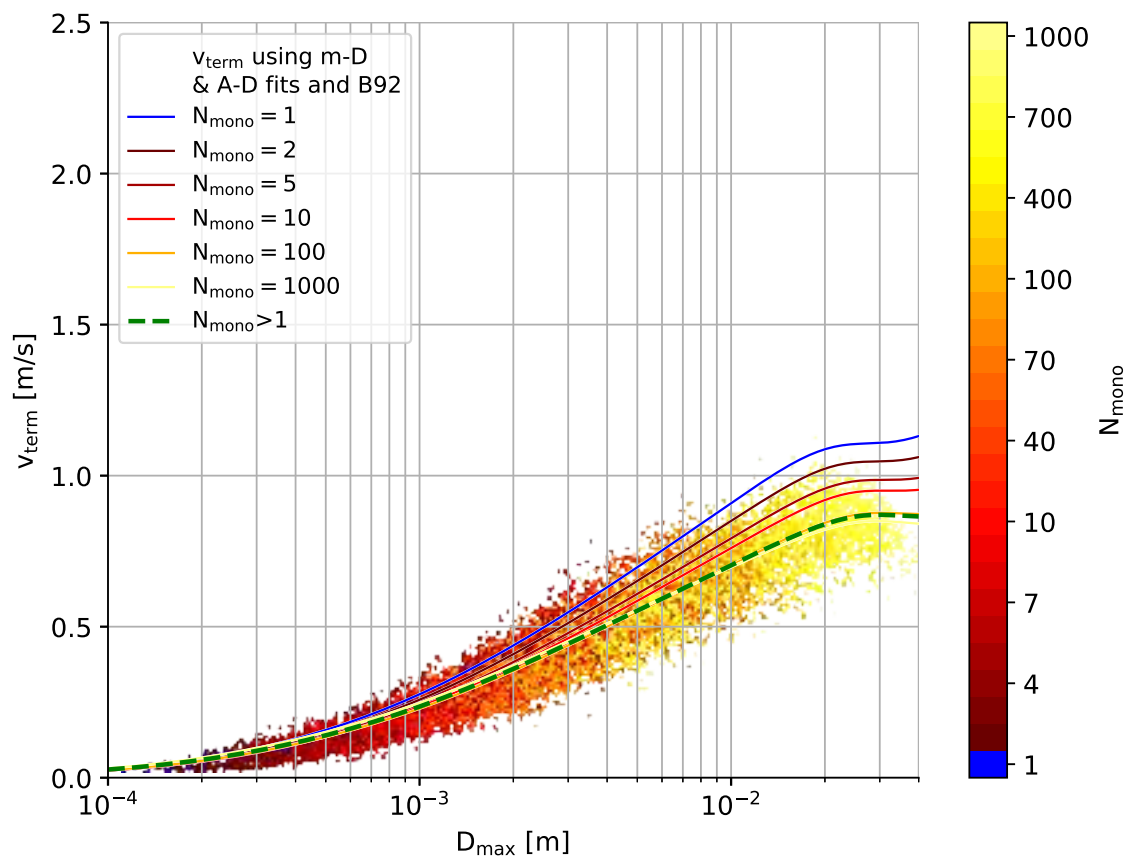


Figure S3. Same as Figure 7 but for aggregates of dendrites

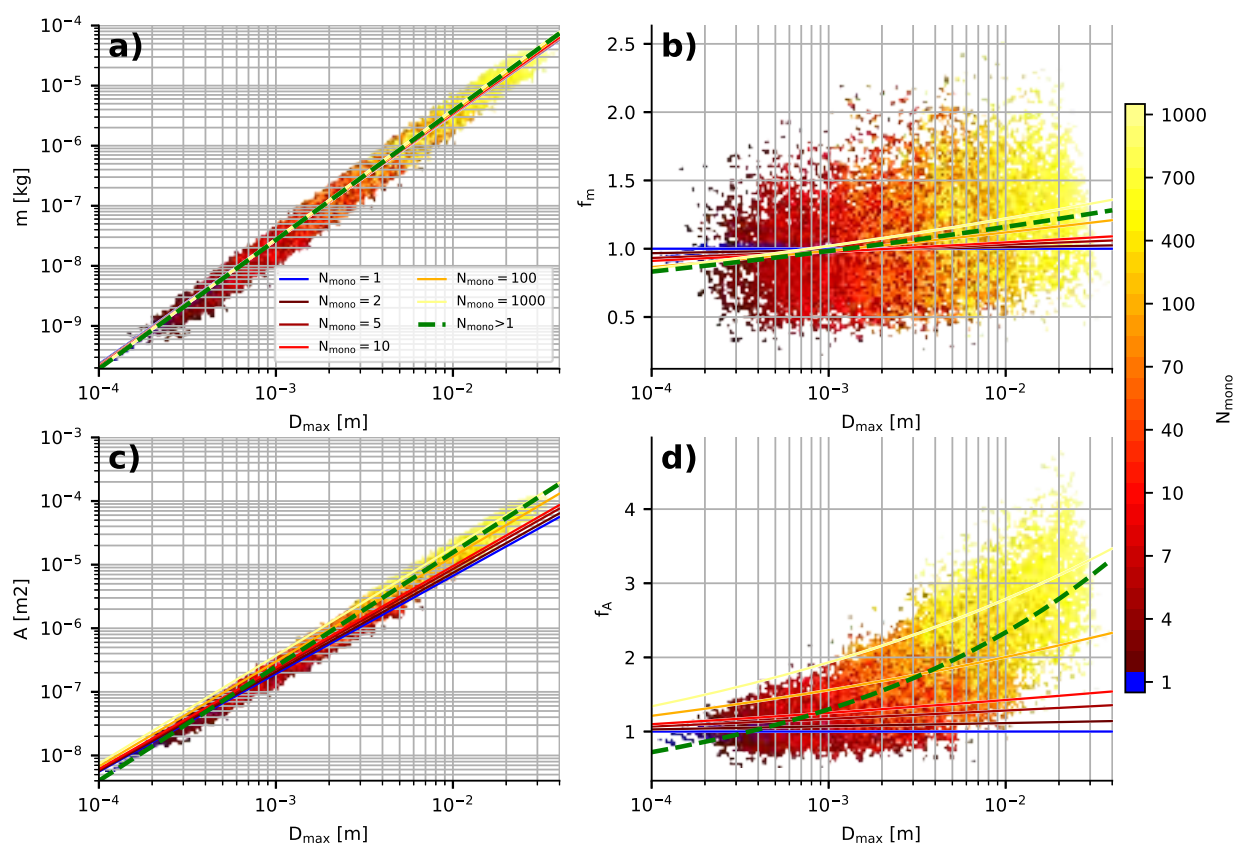


Figure S4. Same as Figure 6 but for aggregates of columns

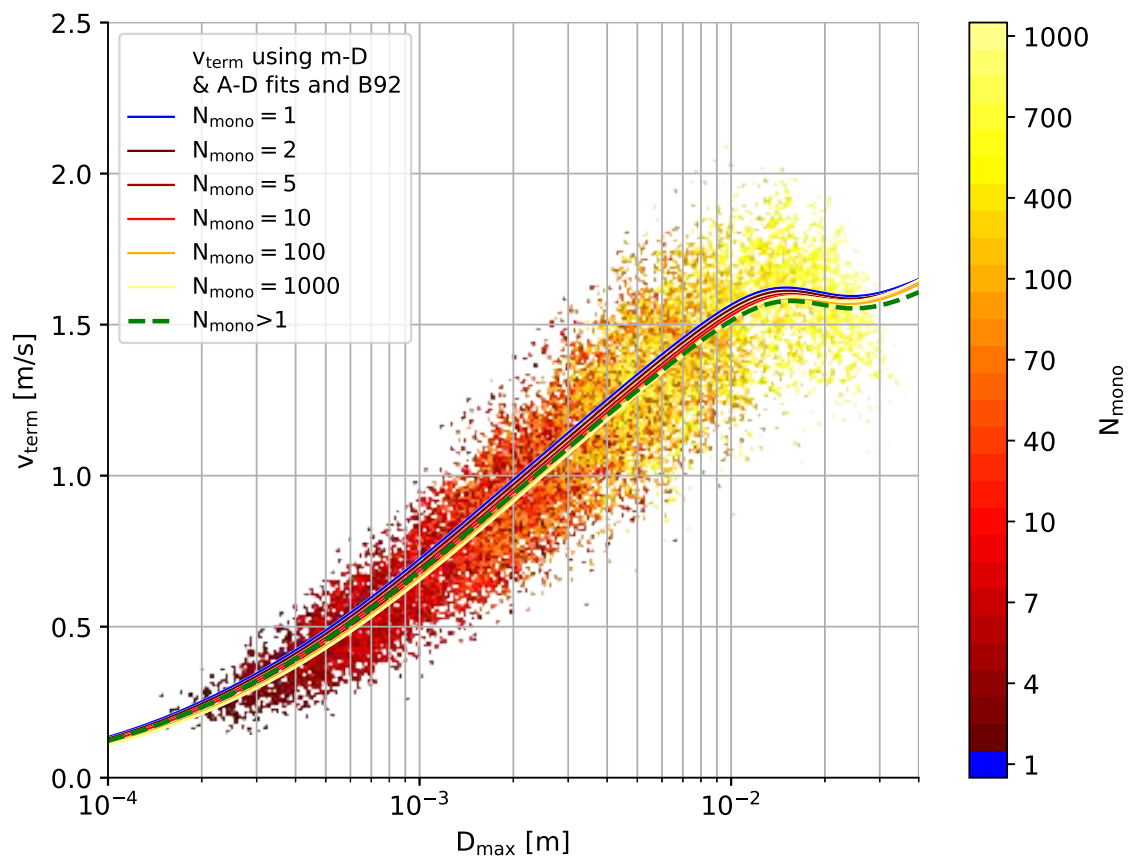


Figure S5. Same as Figure 7 but for aggregates of columns

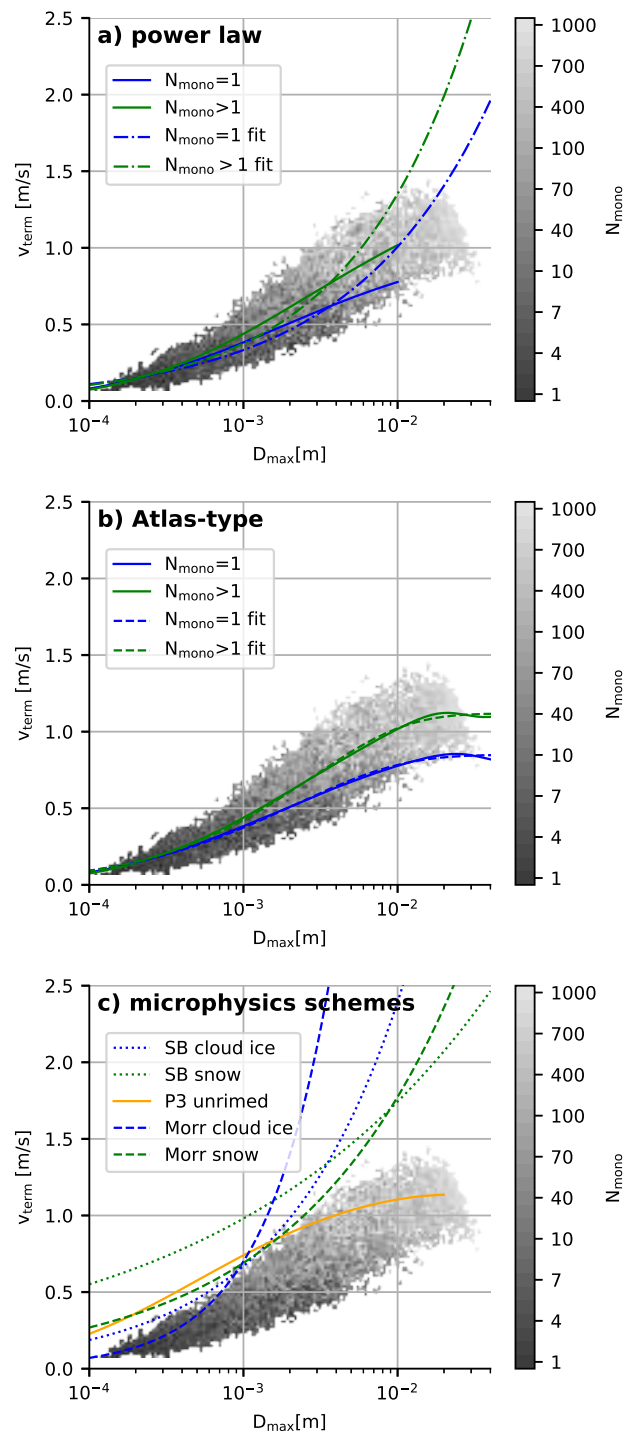


Figure S6. Same as Figure 9 but for aggregates of needles

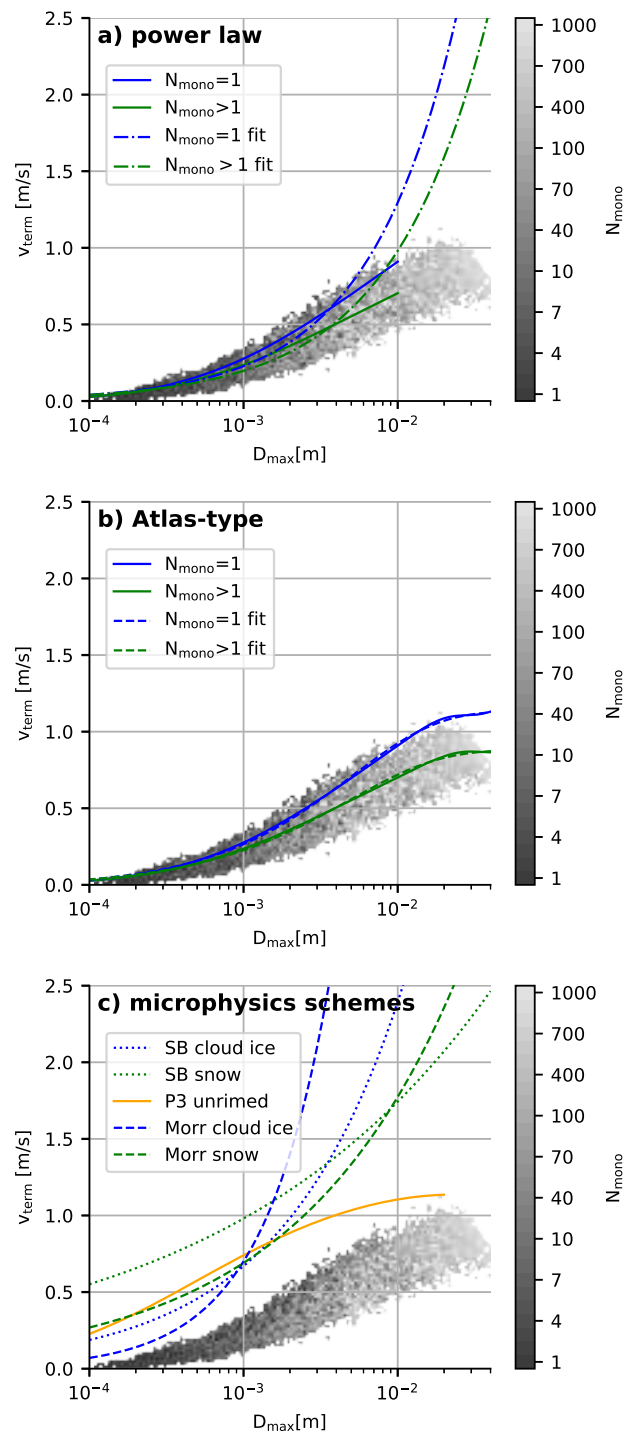


Figure S7. Same as Figure 9 but for aggregates of dendrites

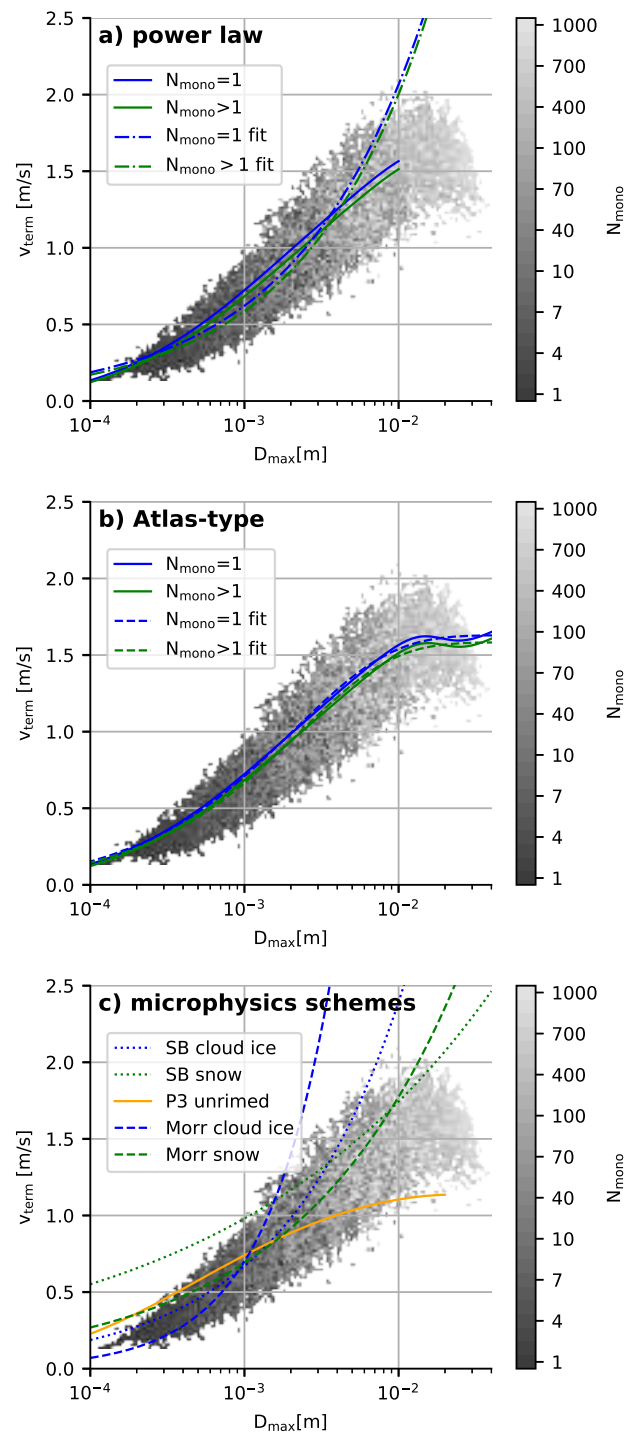


Figure S8. Same as Figure 9 but for aggregates of columns

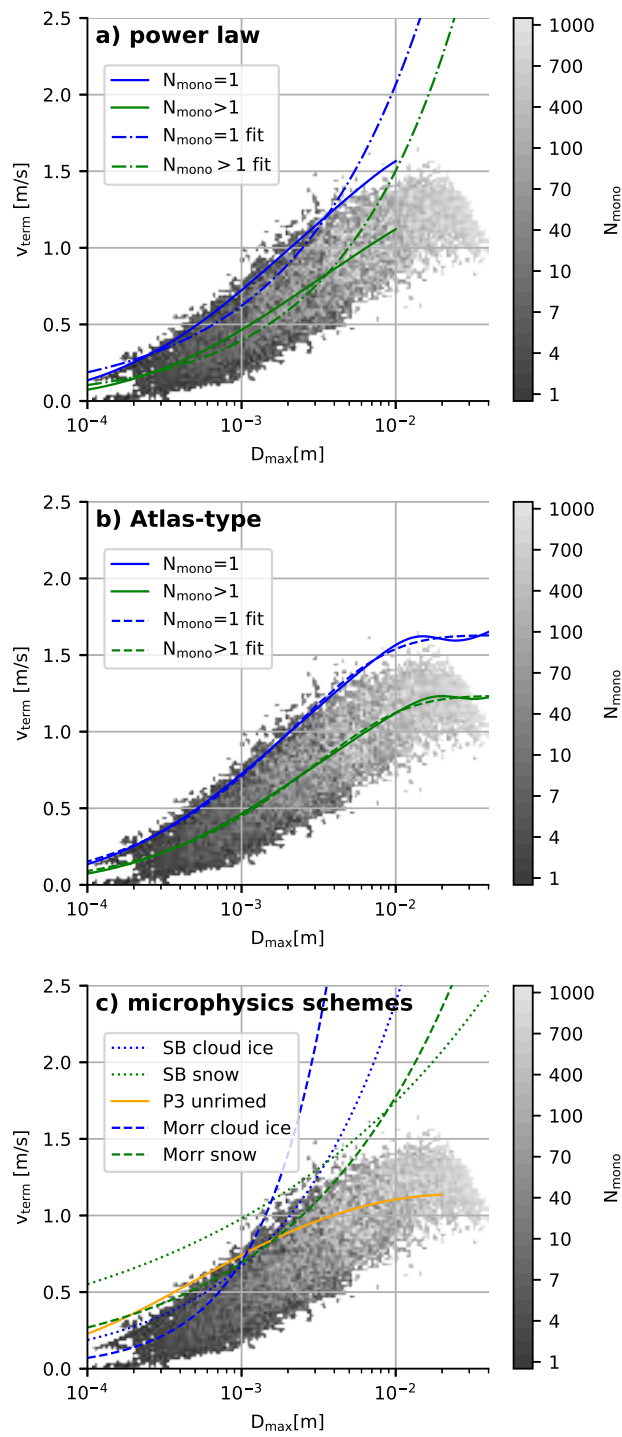


Figure S9. Same as Figure 9 but for "Mix1"

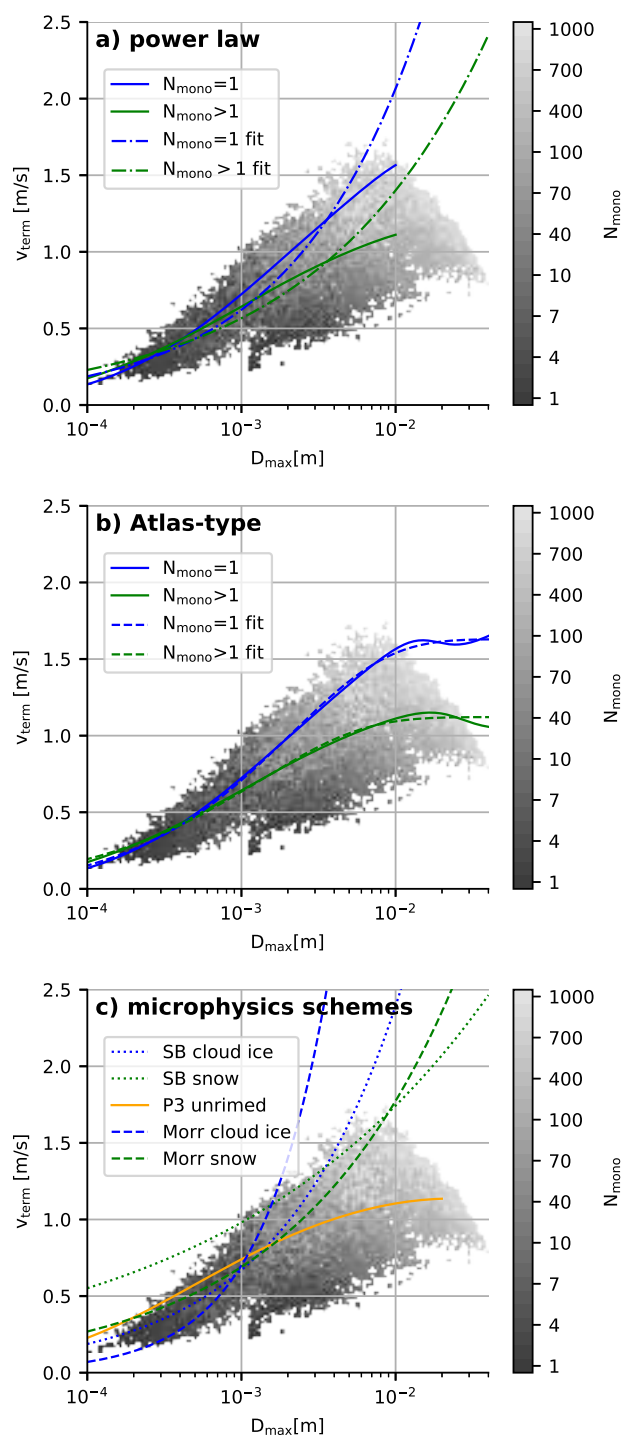


Figure S10. Same as Figure 9 but for "Mix2"

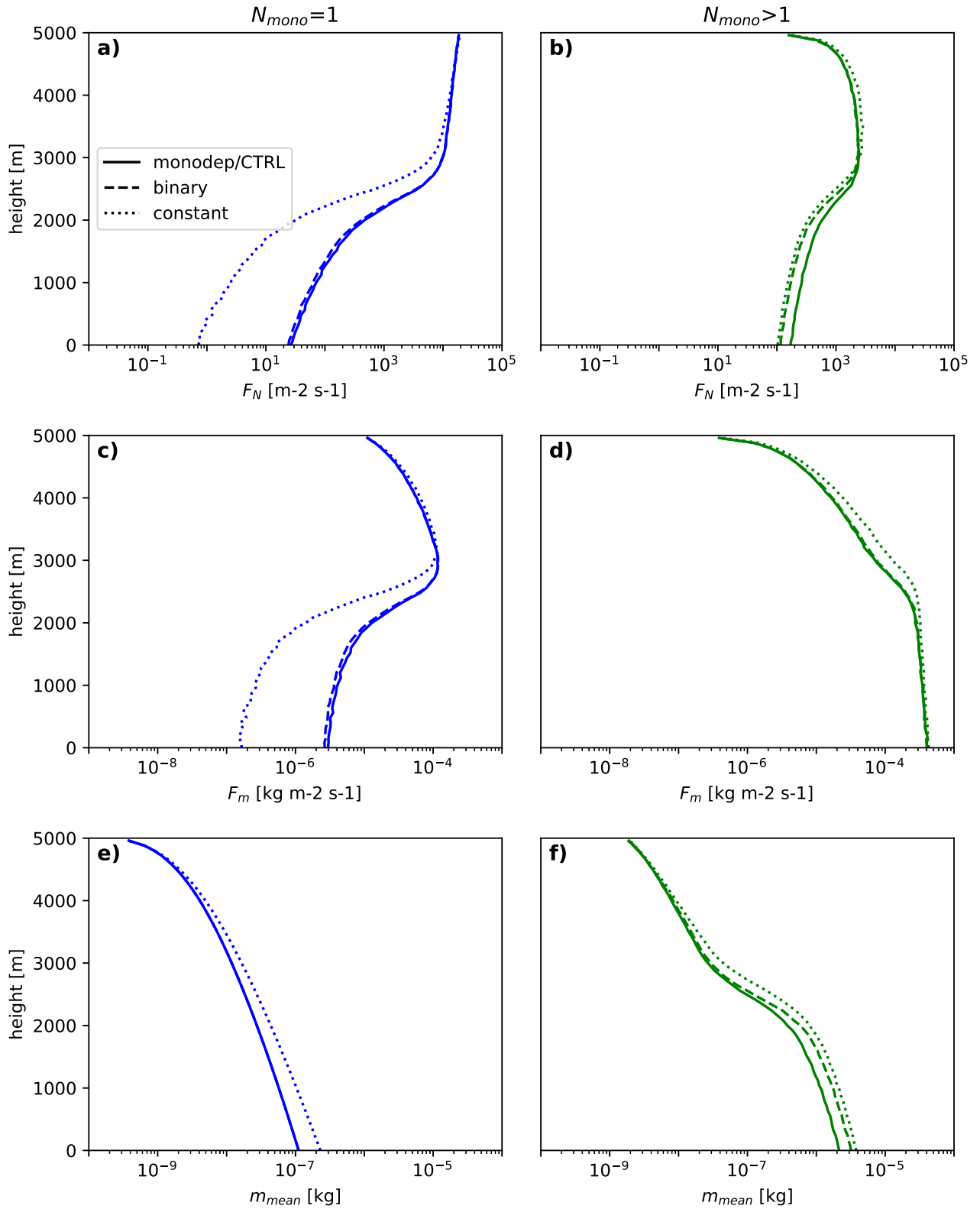


Figure S11. Same as Figure 10 but with a two times smaller mass flux ($F_m = 1 \cdot 10^{-5}$) and same mean mass m_{mean} .

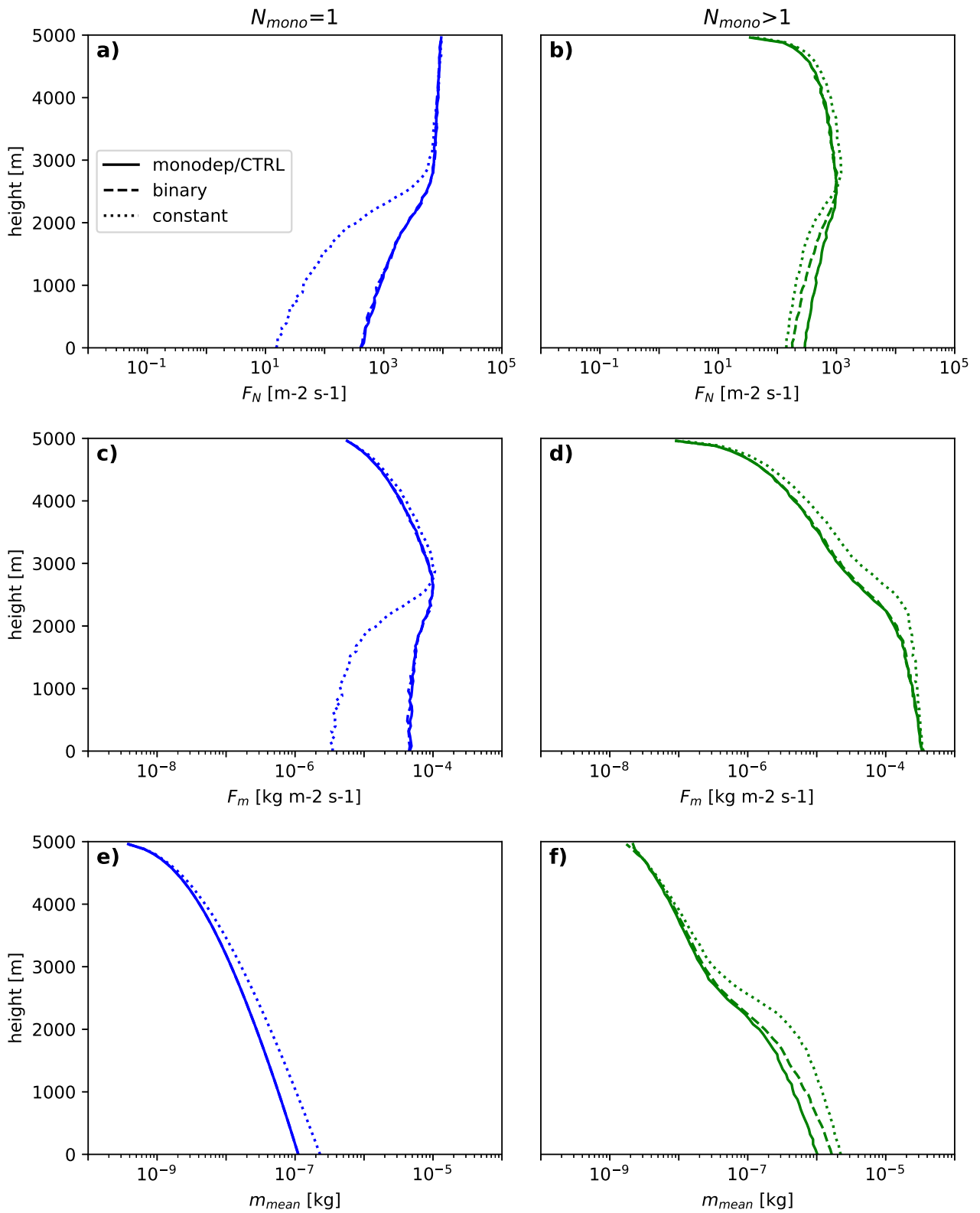


Figure S12. Same as Figure 10 but with a four times smaller mass flux ($F_m = 5 \cdot 10^{-6}$) and same mean mass m_{mean} .

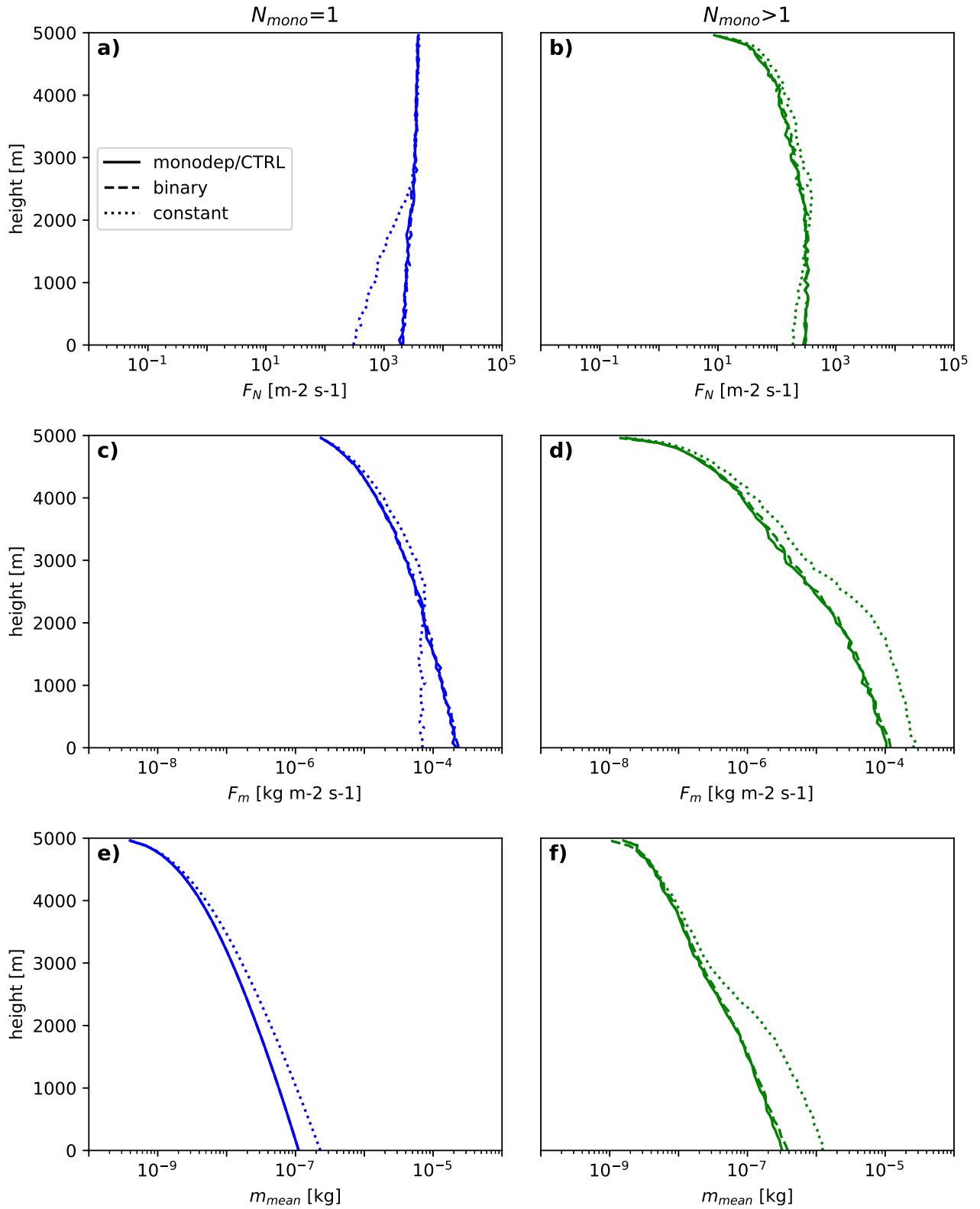


Figure S13. Same as Figure 10 but with a ten times smaller mass flux ($F_m = 2 \cdot 10^{-6}$) and same mean mass m_{mean} .

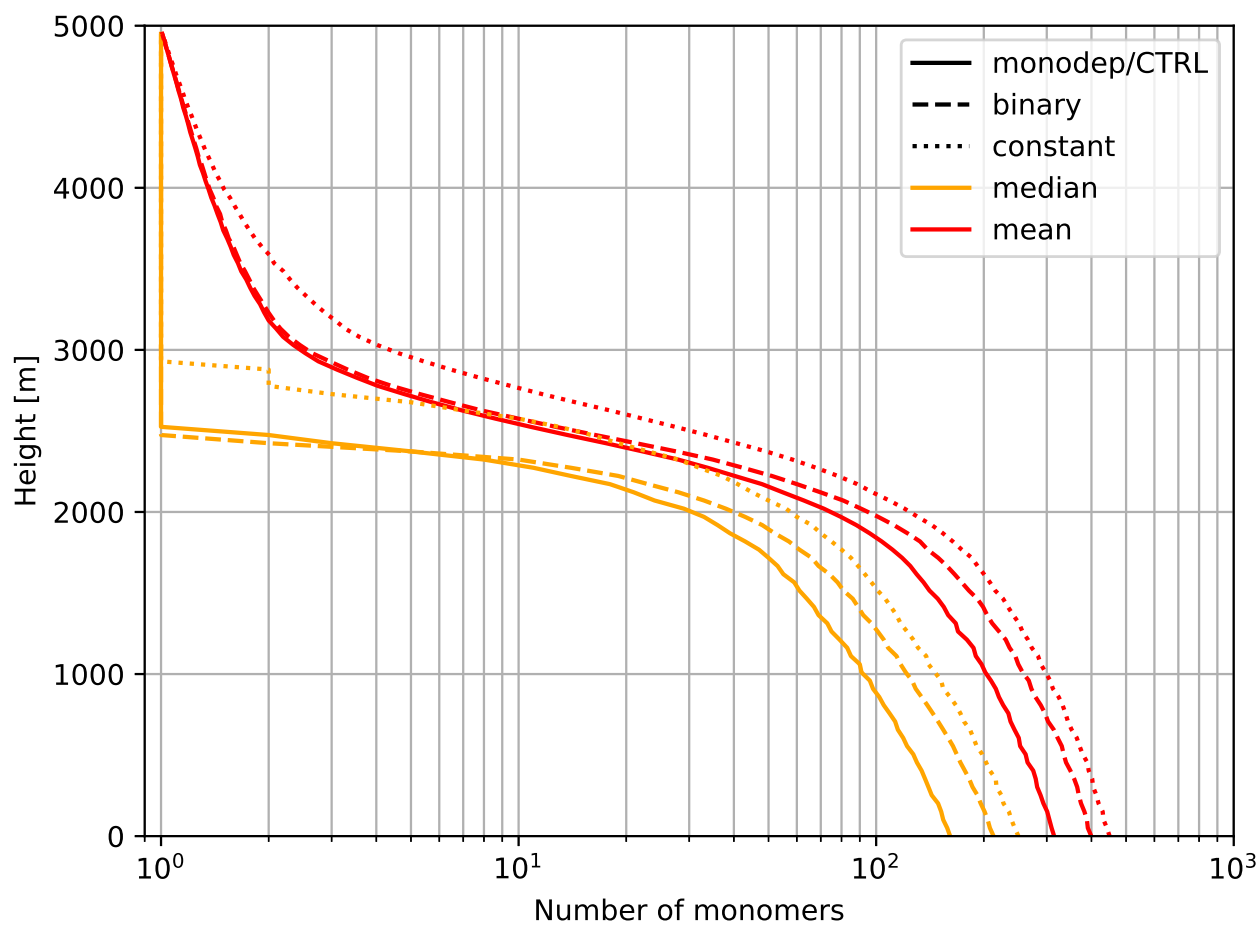


Figure S14. Mean and median N_{mono} corresponding to the simulations shown in Figure 10.

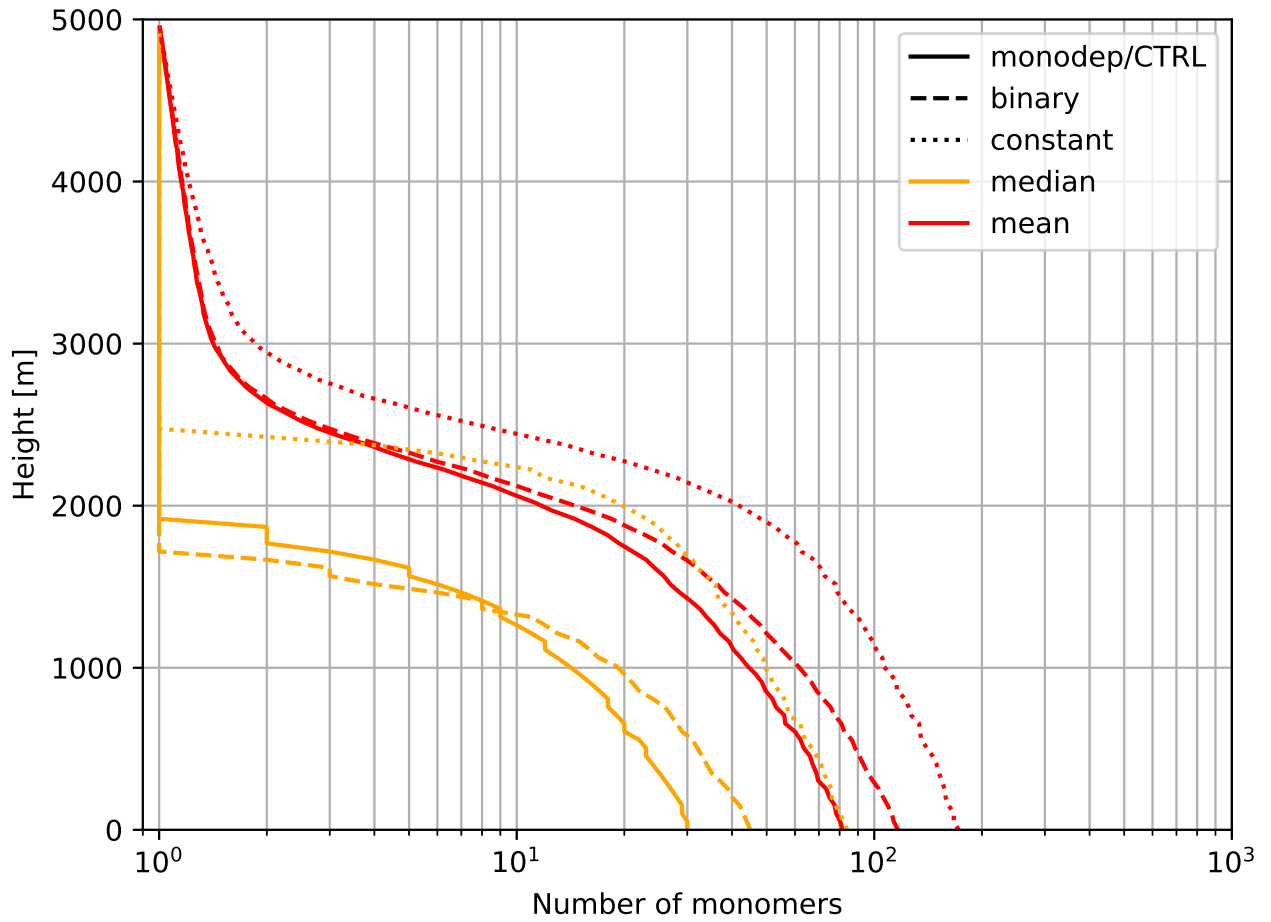


Figure S15. Mean and median N_{mono} corresponding to the simulations shown in Figure S11 but with a two times smaller mass flux ($F_m = 1 \cdot 10^{-5}$) and same mean mass m_{mean} .

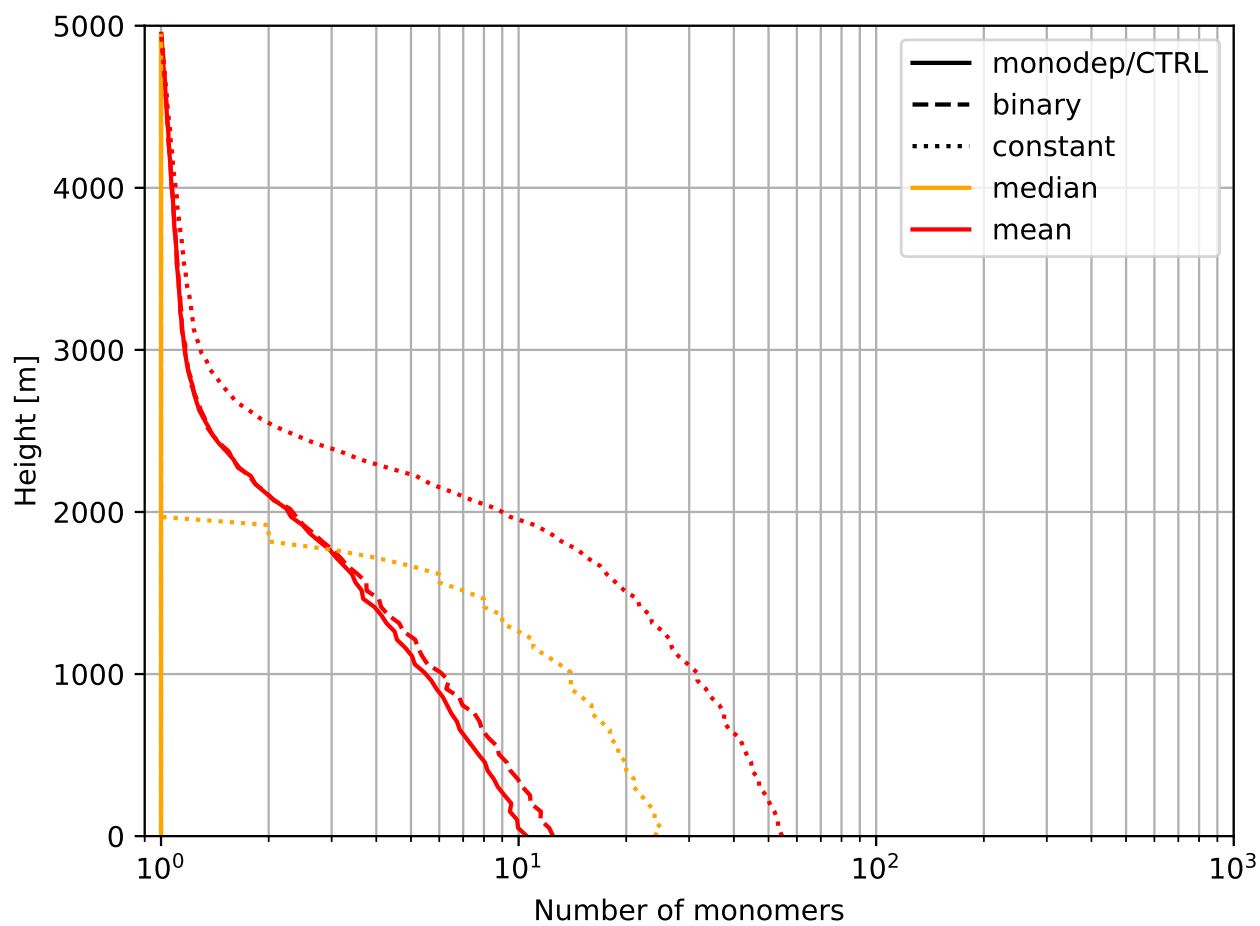


Figure S16. Mean and median N_{mono} corresponding to the simulations shown in Figure S12.

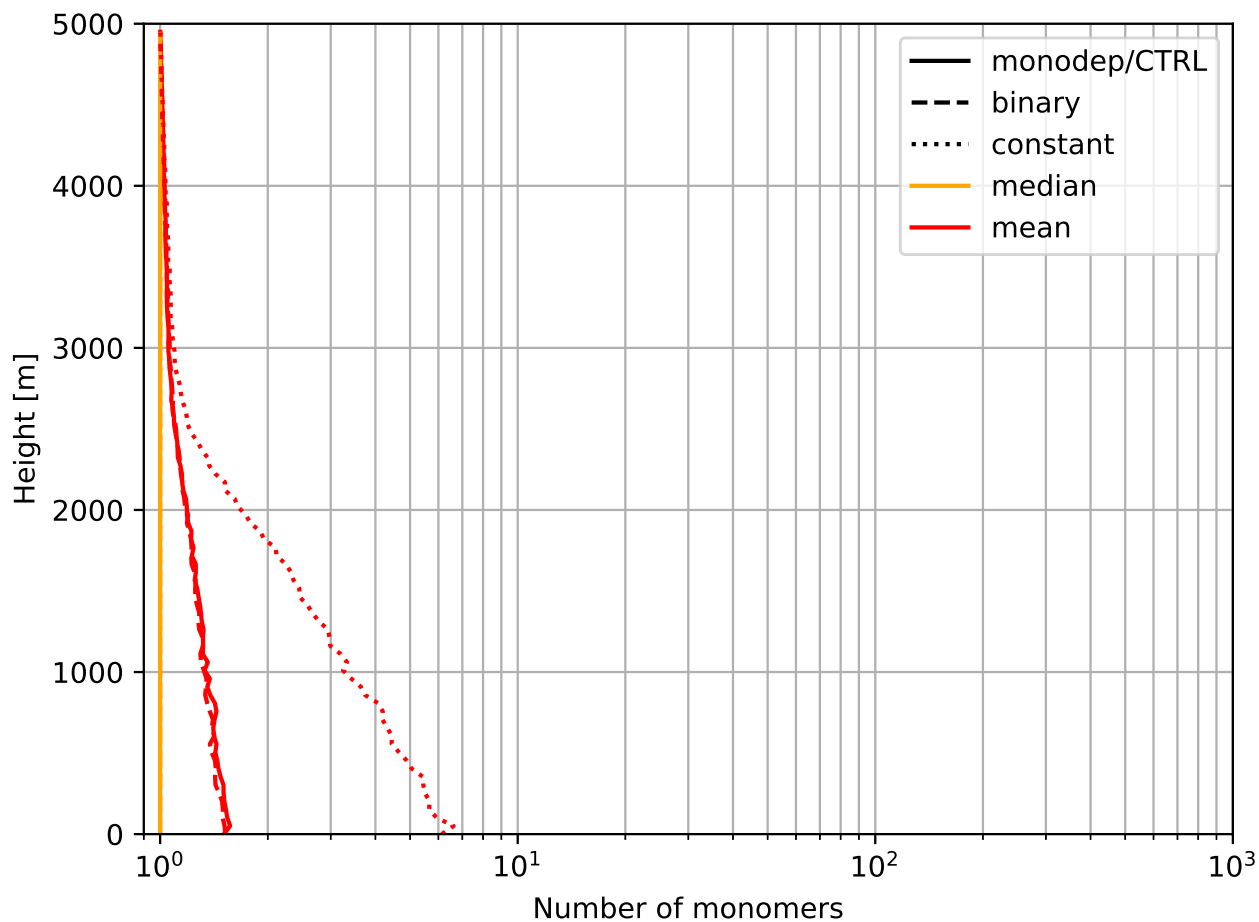


Figure S17. Mean and median N_{mono} corresponding to the simulations shown in Figure S13.